


RESEARCH ARTICLE | SEPTEMBER 11 2023

Nonlinear verification of the resistive-wall boundary modules in the SPECYL and PIXIE3D magneto-hydrodynamic codes for fusion plasmas

L. Spinicci   ; D. Bonfiglio  ; L. Chacón  ; S. Cappello  ; M. Veranda 

 Check for updates

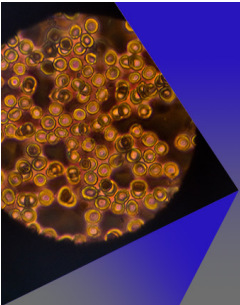
AIP Advances 13, 095111 (2023)

<https://doi.org/10.1063/5.0161029>


View
Online



Export
Citation

CrossMark



AIP Advances
Special Topic: Medical Applications
of Nanoscience and Nanotechnology

Submit Today!



Nonlinear verification of the resistive-wall boundary modules in the SPECYL and PIXIE3D magneto-hydrodynamic codes for fusion plasmas

Cite as: AIP Advances 13, 095111 (2023); doi: 10.1063/5.0161029

Submitted: 7 June 2023 • Accepted: 22 August 2023 •

Published Online: 11 September 2023



View Online



Export Citation



CrossMark

L. Spinicci,^{1,2,a)}  D. Bonfiglio,^{1,3}  L. Chacón,⁴  S. Cappello,^{1,3}  and M. Veranda^{1,3} 

AFFILIATIONS

¹ Consorzio RFX, Euratom-Enea Association, Padua, Italy

² University of Padova, Padua, Italy

³ ISTP, CNR, Milan-Padua-Bari, Italy

⁴ Los Alamos National Laboratory, Los Alamos, New Mexico 87545, USA

^{a)} Author to whom correspondence should be addressed: luca.spinicci@igi.cnr.it

ABSTRACT

A nonlinear verification benchmark is reported between the three-dimensional magneto-hydrodynamic (3D MHD) codes SPECYL [Cappello and Biskamp, Nucl. Fusion **36**, 571 (1996)] and PIXIE3D [Chacón, Phys. Plasmas, **15**, 056103 (2008)]. This work substantially extends a former successful verification study between the same two codes [Bonfiglio *et al.*, Phys. Plasmas, **17**, 082501 (2010)] and focuses on the verification of thin-shell resistive-wall boundary conditions, recently implemented in both codes. Such boundary conditions feature a thin resistive shell in contact with the plasma and an ideal wall placed at a finite distance, separated from the resistive shell by a vacuum region, along with a 3D boundary flow consistent with Ohm's law. This setup allows the study of MHD modes that are influenced by the plasma magnetic boundary, such as external kink modes. The linear growth and nonlinear saturation of external kink modes are studied in both the tokamak and reversed-field pinch magnetic configurations, demonstrating excellent agreement between the two codes. For the tokamak, we present a comparison with analytical linear stability results for the external kink mode, demonstrating remarkable agreement between numerical and analytical growth rates.

© 2023 Author(s). All article content, except where otherwise noted, is licensed under a Creative Commons Attribution (CC BY) license (<http://creativecommons.org/licenses/by/4.0/>). <https://doi.org/10.1063/5.0161029>

I. INTRODUCTION

Advanced computational tools¹ play an increasingly important role in understanding plasma dynamics in magnetic-confinement fusion devices such as the tokamak,² the stellarator,³ and the reversed-field pinch (RFP).^{4,5} The macroscopic properties of fusion plasmas can be fruitfully investigated within a fluid theory approach, where classical fluid dynamics pair with Maxwell equations to produce the magneto-hydrodynamic (MHD) description of the system.^{6,7} Advanced numerical codes designed to solve nonlinear MHD equations in fusion-relevant conditions are fundamental tools to understand and even predict key macroscopic dynamical processes in fusion devices, such as the nonlinear evolution of MHD instabilities such as the kink mode, the tearing mode, or the edge-localized mode. Such plasma instabilities can degrade plasma

confinement, increase the plasma-wall interaction, and possibly produce disruptions,⁸ but when kept at suitable levels, they can also have beneficial effects such as the so-called flux-pumping or MHD dynamo effect,^{9–11} taking advantage of self-organization processes. It is therefore of paramount importance to ensure, on the one hand, that simulation codes provide mathematically correct solutions of the physical models they are based upon and, on the other hand, that such physical models correctly capture the experimental conditions they aim to describe. Such an endeavor is known as verification and validation, and for several years, it has been recognized as a crucial component of magnetic fusion research.¹²

This paper presents the nonlinear verification benchmark of a newly implemented set of resistive thin-shell boundary conditions (BCs) at the edge of the plasma in two nonlinear MHD codes: SPECYL¹³ and PIXIE3D.¹⁴ Capturing the impact of resistive-wall

effects in MHD simulations of magnetic confinement fusion discharges is critical for long-term simulation fidelity as finite-wall resistivity allows for magnetic-field diffusion across the wall that impacts both plasma stability and confinement. However, the thin-shell resistive-wall treatment is highly nontrivial and benefits particularly from a detailed code-to-code comparison such as the one undertaken here, which will also serve as a reference for future implementation as well. This work comes as a substantial extension of a former successful verification study between the two codes, which presented completely different numerical implementations (spectral vs finite differences) and was published in Ref. 15. There, a simplified set of BCs was used in both codes, featuring an ideally conducting shell in direct contact with the plasma. The present implementation considers a more realistic boundary, with a resistive thin shell in contact with the plasma and a vacuum region outside it, up to an ideal wall placed at a finite, tunable distance from the plasma, as shown schematically in Fig. 1. Full consistency with the plasma Ohm's law is achieved through a 3D boundary flow instead of the usual "rigid shell" assumption that explicitly enforces zero finite radial velocity at the plasma edge. The resistive penetration time of the shell can be varied from much longer than the Alfvén time scale (thus recovering ideal shell conditions) to much shorter (corresponding to a free interface between the plasma and the vacuum region). The new set of BCs makes it possible to study the influence of a finite-resistivity plasma boundary on MHD mode dynamics, such as the external kink mode (which becomes unstable when the plasma-shell proximity, defined as the ratio between the ideal shell position b and the plasma radius a , exceeds a given threshold⁶).

In the previous ideal-wall verification study,¹⁵ a range of RFP and tokamak configurations were examined with both SPECYL and PIXIE3D in one-, two-, and three-dimensions (1D, 2D, and 3D). The linear growth rates of unstable modes were found to agree within 0.3%, and overall excellent agreement of the solutions was shown in the nonlinear regime. The present verification study will build on this earlier exercise to focus on the verification of the new set of thin-shell resistive-wall (RW) BCs in 2D helical geometry, in which the ratio of toroidal to poloidal mode periodicity is fixed. We will show that excellent agreement is again obtained between the

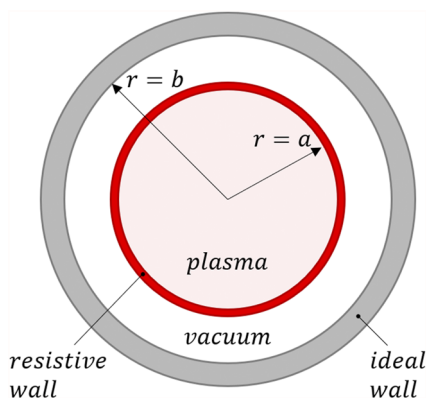


FIG. 1. Schematic view of the resistive-wall BCs implemented in SPECYL and PIXIE3D. A thin resistive shell is placed at the plasma boundary $r = a$ and is surrounded by a vacuum region enclosed by an ideal wall at $r = b$.

two codes with the new set of RW BCs and that numerical results are remarkably consistent with expectations from linear stability theory.

The paper is organized as follows: Sec. II gives an overview on the two codes. In Sec. III, we summarize the main features of the new RW BC implementation in SPECYL and PIXIE3D. Section IV discusses the numerical setup of the proposed verification tests and details of the verification process. The numerical results are reported in Sec. V. Finally, we summarize and make closing remarks in Sec. VI. Four appendices are also presented: a brief overview of the workflow of the SPECYL code (Appendix A) and the detailed derivation of the normal- \mathbf{B} time-evolution equation (Appendix B), of the RW magnetic response (Appendix C), and of the analytical decay rate of a magnetic signal on a thin RW immersed in vacuum (Appendix D). The latter provides a benchmark for the double-vacuum analytical study presented in Sec. V A.

II. OVERVIEW OF SPECYL AND PIXIE3D CODES

A. SPECYL

The spectral cylindrical code SPECYL solves the compressible visco-resistive nonlinear MHD model in a negligible-pressure, constant-density limit. It evolves with respect to time t , magnetic field \mathbf{B} , and flow velocity \mathbf{v} according to the following set of equations:

$$\rho(\partial_t \mathbf{v} + \mathbf{v} \cdot \nabla \mathbf{v}) = \mathbf{J} \times \mathbf{B} + \rho \nu \nabla^2 \mathbf{v}, \quad (1)$$

$$\partial_t \mathbf{B} = -\nabla \times \mathbf{E}, \quad (2)$$

$$\mathbf{E} = \eta \mathbf{J} - \mathbf{v} \times \mathbf{B}, \quad (3)$$

$$\mathbf{J} = \nabla \times \mathbf{B}, \quad (4)$$

$$\nabla \cdot \mathbf{B} = 0. \quad (5)$$

In the above-mentioned equations, ρ is the plasma density, \mathbf{J} is the current density, ν is the kinematic viscosity, η is the plasma resistivity, and \mathbf{E} is the electric field. All quantities are normalized and appear in dimensionless form. In particular, the lengths are normalized to the plasma minor radius a , the plasma density is normalized to the initial ion density on axis $n_0 m_i$, the magnetic field is normalized to its initial value on axis B_0 , the velocity is normalized to the Alfvén velocity $v_A = B_0 / (\mu_0 n_0 m_i)^{1/2}$, where μ_0 is the plasma permeability and m_i is the ion mass, and time is normalized to the Alfvén time $\tau_A = a / v_A$. In these units, the resistivity η corresponds to the inverse Lundquist number $S^{-1} = \tau_A / \tau_R$ (with $\tau_R = \mu_0 a^2 / \eta$ being the resistive time-scale), and the kinematic viscosity ν corresponds to the inverse viscous Lundquist number $M^{-1} = \tau_A / \tau_\nu$ (with $\tau_\nu = a^2 / \nu$ being the viscous time-scale). ρ , η , and ν are assumed to be constant in time and can be assigned a radial dependence (see, e.g., Ref. 16 for a modeling study with SPECYL using a non-uniform density profile). In this study, we assume that ρ and ν are spatially uniform, and we only assign a radially increasing dependence to the resistivity, consistent with the initial axisymmetric Ohmic equilibrium, so that the resistivity just inside the wall is 20 to 100 times larger than that in the core, depending on the cases (see Sec. IV).

The geometry is that of a periodic cylinder, of radius a and of height $2\pi R$ (R being the plasma major radius), having coordinates (r, θ, z) . The code uses finite differences in the radial coordinate r and a spectral formulation in the periodic coordinates θ and z . The time-stepping is semi-implicit and proceeds with a predictor-corrector scheme, as described in [Appendix A](#). The most general implementation of the SPECYL code features a semi-implicit term in the momentum balance equation, much similar to the isotropic operator in [Ref. 17](#). In the present work, however, this term is not used to avoid any possible effect on the verification results. This is made possible by using sufficiently small time steps, similar to what was done in [Ref. 15](#).

B. PIXIE3D

The conservative, fully implicit finite-difference code PIXIE3D^{14,18} is based on a more complete visco-resistive compressible nonlinear MHD model, allowing barotropic pressure p and time variation of density. The full set of equations, written in conservative form and normalized the same way as Eqs. (1)–(5), reads

$$\partial_t \rho + \nabla \cdot (\rho \mathbf{v}) = 0, \quad (6)$$

$$\partial_t (\rho \mathbf{v}) + \nabla \cdot \left[\rho \mathbf{v} \mathbf{v} - \mathbf{B} \mathbf{B} - \rho \nu \nabla \mathbf{v} + \mathbb{I} \left(p + \frac{B^2}{2\mu_0} \right) \right] = 0, \quad (7)$$

$$\partial_t \mathbf{B} = -\nabla \times \mathbf{E}, \quad (8)$$

$$\mathbf{E} = \eta \mathbf{J} - \mathbf{v} \times \mathbf{B} - \frac{d_i}{\rho} (\mathbf{J} \times \mathbf{B} - \nabla p_e), \quad (9)$$

$$\mathbf{J} = \nabla \times \mathbf{B}, \quad (10)$$

$$\nabla \cdot \mathbf{B} = 0, \quad (11)$$

$$\partial_t T_e + \mathbf{v}_e \cdot \nabla T_e + (\gamma - 1) \left[T_e \nabla \cdot \mathbf{v}_e + \frac{\nabla \cdot \mathbf{q} - \mathbf{Q}}{\rho} \right] = 0, \quad (12)$$

$$p_e = \rho T_e; \quad p = (1 + \alpha_T) p_e; \quad \mathbf{v}_e = \mathbf{v}_i - \frac{d_i}{\rho} \mathbf{J}, \quad (13)$$

where \mathbf{v}_i is the ion velocity, $\mathbf{v} \approx \mathbf{v}_i$ is the bulk plasma flow, $d_i = c/\omega_{pi}$ is the ion skin depth, T_e is the electron temperature, $\alpha_T = T_i/T_e$ is the ratio of ion to electron temperatures (assumed constant), and \mathbb{I} is the identity tensor. The electric field is determined by resistive Ohm's law⁷ plus a Hall term, accounting for the interaction between the two plasma species.¹⁴ Resistivity and viscosity are, in principle, functions of the plasma state (ion/electron temperatures, density, etc.). The plasma temperature $T = (1 + \alpha_T) T_e$, which is governed by the heat equation [Eq. (12)], with \mathbf{q} and \mathbf{Q} being the heat flux and heat source, respectively, and γ being the polytropic constant ($p \propto \rho^\gamma$).

In this study, we will consider $d_i = 0$, $\gamma = 1$, $\alpha_T = 1$, and $\mathbf{q} = 0$; in this case, Eq. (13) expresses the isothermal equation of state for the two-species plasma, and $p = 2\rho T_e$. Moreover, ν is assumed to be constant in time and spatially uniform, T_e is assumed to be negligible, and η is assumed to follow a specified radial dependence as in

SPECYL. In addition, ρ is taken to be constant and uniform. Indeed, the continuity equation in the simple form of Eq. (6) with a purely radial pinch flow would produce a singular mass-density profile on the axis. The singularity is typically regularized by introducing *ad hoc* diffusion coefficients¹⁹ to redistribute the mass-density into a non-singular, smooth profile. The approach typically used in SPECYL (and also in this verification study) is to assume *a priori* a constant and uniform mass-density profile. Despite its simplicity, this assumption (also discussed in Sec. 9.3.3 of [Ref. 20](#)) is reasonable for two reasons. First, it agrees with experimental observations reasonably well, especially in the RFPs, where the plasma density is typically uniform (see, e.g., [Ref. 21](#)). Second, due to the zero- β assumption, only current-driven instabilities are of concern in this article, which are largely unaffected by mass density evolution. Indeed, as will be shown in this article, excellent agreement is found with the linear theory analysis (which does not explicitly enforce the constant-density assumption) of $m = 1$ external kink modes in the tokamak case. With these assumptions, the equations solved by the two codes become identical, as required for the purpose of the verification benchmark.

PIXIE3D adopts a conservative, solenoidal finite-difference scheme¹⁸ to discretize the equations using a uniform rectangular logical grid ξ that remains uniform and Cartesian at all times. This is then embedded into the real space geometry through a change of coordinates $\mathbf{x} = \mathbf{x}(\xi)$. The generalized curvilinear approach makes PIXIE3D capable of coping with many different geometries, e.g., helical, cylindrical, and toroidal, relevant for fusion. In this study, 2D helical geometry is used throughout: $\mathbf{x}(\xi)$: $\{r, u, z\} \rightarrow \{r \cos((u + kz)/m), r \sin((u + kz)/m), z\}$, with $u = m\theta - kz$ (where m and $k = n/R$ define the helical pitch).

Temporal discretization is fully implicit using either the Crank–Nicolson or a second-order backward differentiation formula. The resulting set of algebraic equations is then treated iteratively with a preconditioned Newton–Krylov solver.^{18,22} This choice provides good algorithmic scalability and allows relatively larger time steps with respect to SPECYL.

Finally, PIXIE3D provides two alternative formulations, dubbed here PIXIE3D-A and PIXIE3D-B, solving Eqs. (6)–(13) for the magnetic potential \mathbf{A} and the magnetic field \mathbf{B} . The magnetic vector potential equation (in the Weyl gauge with zero electrostatic potential) reads

$$\partial_t \mathbf{A} + \mathbf{E} = 0. \quad (14)$$

III. RESISTIVE THIN-SHELL BOUNDARY CONDITIONS

A. Magnetic field components

1. Physical derivation

We seek a well-posed set of RW BCs for curvilinear geometries. This is well documented in the literature^{23–28} and has already been implemented in other codes^{29–44} in cylindrical, toroidal, or local-Cartesian coordinates. In this study, we only consider cylindrical/helical coordinates. However, PIXIE3D supports general coordinates,¹⁸ which we consider in this section for generality.

Next, we derive the set of magnetic-field, thin-shell RW BCs. We consider the flow RW BCs in [Sec. III B](#). The resistive-wall dynamics are driven by the electric field supported by it, which are computed from Ampère's and Ohm's equations as

$$\mathbf{E}_w = \eta_w \mathbf{J}_w,$$

with \mathbf{E}_w and \mathbf{J}_w being the electric field and the current density at the wall, respectively, and η_w being the resistivity of the wall. In curvilinear geometry, we have

$$\begin{aligned} E_w^2 &= \eta_w / \mu_0 [\partial_3 B_1 - \partial_1 B_3], \\ E_w^3 &= \eta_w / \mu_0 [\partial_1 B_2 - \partial_2 B_1], \end{aligned}$$

where superindices mark contravariant components and subindices mark covariant ones (using the convention in Ref. 18). We assume a thin wall of thickness δ_w , within which the electric field is constant (so-called “thin-wall” approximation²³). Integrating the above-mentioned equations across the wall ($\int_{\xi_w^-}^{\xi_w^+} d\xi_1$), we find

$$E_w^2 = -\frac{a}{|\mathbf{n}| \tau_w} [B_3]_-^+ = -\frac{a}{|\mathbf{n}| \tau_w} \delta B_3, \quad (15)$$

$$E_w^3 = \frac{a}{|\mathbf{n}| \tau_w} [B_2]_-^+ = \frac{a}{|\mathbf{n}| \tau_w} \delta B_2, \quad (16)$$

where $\tau_w = (\mu_0 \nu_A \tau_A \delta_w / \eta_w)$ is the wall resistive time, $|\mathbf{n}| = |\nabla \xi_n| \approx \delta \xi_w / \delta_w$ (with $\delta \xi_w = \xi_w^+ - \xi_w^-$ and δ_w being the wall thickness) is the magnitude of the normal vector to the resistive wall, and we have shortened the notation as $\xi_w^\pm \rightarrow \pm$. Note that this result can be rewritten as

$$\mathbf{E}_w = \mathbf{E}_0 + \frac{a}{|\mathbf{n}| \tau_w} \mathbf{n} \times \delta \mathbf{B}_t = \mathbf{E}_0 + \frac{a}{\tau_w} \hat{\mathbf{n}} \times \delta \mathbf{B}_t, \quad (17)$$

where $\delta \mathbf{B}_t = [\mathbf{B}_t]_-^+$, $\hat{\mathbf{n}} = \mathbf{n} / |\mathbf{n}|$, and we have added an imposed electric field, \mathbf{E}_0 , to allow for an external loop voltage to drive the simulation.

Once the wall electric-field is known, the evolution equation for the normal- \mathbf{B} component can be derived by plugging Eq. (17) into Faraday’s law at the resistive wall radius, giving

$$\partial_t (\mathbf{n} \cdot \mathbf{B})_a + \frac{a}{\tau_w} \nabla \cdot [|\mathbf{n}| \delta \mathbf{B}_t]_a = 0, \quad (18)$$

where the subscript “ a ” indicates evaluation at the wall radius $r = a$. The divergence of the tangential magnetic field components can then be written in terms of the normal component using the solenoidal property of the magnetic field. This gives the evolution equation for the normal magnetic field component (see Appendix B).

The boundary conditions for the tangential magnetic field components are determined using the resistive Ohm’s law and the plasma momentum equation (plasma inertia and viscosity effects at the boundary are neglected for the time being $\mathbf{J} \times \mathbf{B} \approx \nabla p$, but these approximations can be relaxed, if needed, by adding the corresponding terms to the ∇p term below), giving¹⁹

$$\mathbf{J}_t = \lambda \mathbf{B}_t + \frac{\mathbf{B} \times \nabla p}{B^2}, \quad \text{with} \quad \lambda = \frac{\mathbf{E}_w \cdot \mathbf{B}}{\eta |\mathbf{B}|^2}. \quad (19)$$

In the zero- β case, $\nabla p = 0$, and the condition $\mathbf{J}_t \times \mathbf{B}_t = 0$ is strictly enforced. This treatment has proven sufficient in the context of this study to prevent the formation of numerically induced boundary

layers at the RW. Equations (18) and (19) are a well-posed set of magnetic field RW boundary conditions.

Equation (19) had already been implemented in PIXIE3D and SPECYL to deal with discharges driven by an external loop voltage, and therefore, all that is needed to deal with resistive shells is the computation of the RW electric field and the normal- \mathbf{B} update. Equation (17) indicates that the boundary tangential electric field must be computed from the jump in the tangential magnetic field components at the resistive wall. This, in turn, requires the computation of the external magnetic field in the vacuum region between the plasma resistive wall (at $r = a$) and the ideal wall (at $r = b$). The normal (contravariant) magnetic field components are continuous across the resistive wall, owing to the solenoidal property of the magnetic field, i.e.,

$$B^{n,+} = B^{n,-}. \quad (20)$$

In vacuum, the current density is zero, and hence, $\mathbf{B} = \nabla \Phi$, where Φ is a scalar potential. The solenoidal condition then implies that

$$\nabla^2 \Phi = 0$$

in the vacuum region, subject to boundary conditions enforcing continuity of the normal magnetic field at the resistive wall [Eq. (20)] and a perfect conductor at the outer ideal wall ($B_n = 0$).

In the cylindrical/helical geometries considered in this paper, the vacuum-region boundary conditions read

$$\partial_r \Phi|_{r=a} = B_r^+; \quad \partial_r \Phi|_{r=b} = 0.$$

The corresponding vacuum Laplace equation can be solved analytically²⁹ using Fourier decomposition, and the Fourier amplitudes of the non-axisymmetric vacuum magnetic field components generated by the RW obey the following relations:

$$\left(\frac{B_\theta^{m,n}}{i B_r^{m,n}} \right)_+ = \Theta_{m,n}(a, b), \quad \left(\frac{B_z^{m,n}}{i B_r^{m,n}} \right)_+ = Z_{m,n}(a, b), \quad (21)$$

where $\Theta_{m,n}(a, b)$ and $Z_{m,n}(a, b)$ are reported in Appendix C and can be shown to be consistent with the solenoidal property of the vacuum field at the wall. The axisymmetric component of the RW magnetic response is consistent with the previous ideal wall implementation (see Appendix C) and is treated accordingly in both codes.

Next, we describe the specific implementation details of the magnetic-field RW boundary conditions in PIXIE3D and SPECYL. Both in PIXIE3D and SPECYL, τ_w is treated as an input parameter. According to its value, we can isolate two interesting limit cases:

- *vacuum-wall* ($\tau_w \leq \tau_A$): resistive magnetic-diffusion through the RW is almost instantaneous on the simulation time scales; hence, the boundary is transparent to the electro-magnetic fields and can be considered as a free plasma-vacuum interface (the so-called “vacuum wall” in Ref. 24);
- *ideal-wall* ($\tau_w \gg$ simulation time): the wall behaves like an ideal conductor, and no magnetic-field diffusion can take place on the simulation time scale.

2. Implementation in PIXIE3D

The RW treatment in PIXIE3D begins by computing the RW electric field \mathbf{E}_w at the beginning of each time-step using the prior-step values of the plasma magnetic field. This wall electric field is then used for the next time step. This is an explicit temporal update, which features a stability time step limit of the form (in cylindrical geometry)

$$\Delta t \lesssim 0.5 \Delta r \tau_w. \quad (22)$$

This time step limit is generally not problematic for sufficiently large resistive-wall times, but it can become quite limiting for small τ_w .

The vacuum magnetic field response in cylindrical/helical geometry is implemented in a pseudo-spectral fashion by performing an FFT of the normal magnetic field component along the azimuthal direction and then computing the tangential components through the $\Theta_{m,n}$ and $Z_{m,n}$ coefficients. From these, it can be seen that \mathbf{E}_w follows from Eq. (17) after an inverse FFT procedure to recover fields on the mesh. In more general geometries, a vacuum magnetic-field solver will be required to compute the tangential magnetic field components from the normal one. The resistive-wall treatment on the plasma side is already suitable for arbitrary geometries.

PIXIE3D already implements the tangential- \mathbf{B} BCs in Eq. (19).¹⁹ In PIXIE3D-A, normal- \mathbf{B} is evolved by updating the tangential components of \mathbf{A} according to Eq. (14),

$$\partial_t (\mathbf{n} \times \mathbf{A})_a + (\mathbf{n} \times \mathbf{E})_a = 0, \quad (23)$$

which is advanced explicitly as (here, k is the time level)

$$\mathbf{n} \times \mathbf{A}|_a^{k+1} = \mathbf{n} \times \mathbf{A}|_a^k - \Delta t (\mathbf{n} \times \mathbf{E}^k)_a. \quad (24)$$

An implicit update is, in principle, possible but cumbersome, and it is of no practical advantage in the usual case of $\tau_w/\tau_A \gg 1$. No boundary condition is formally needed for the normal \mathbf{A} -component, but we fill the corresponding ghost-cell from the tangential ones using $\nabla \cdot \mathbf{A} = 0$ for consistency with the Coulomb gauge employed in the divergence-cleaning procedure explained below.

In PIXIE3D-B, one can, in principle, use Eq. (18) directly to update the normal- \mathbf{B} component at the boundary, as is done in other MHD codes.^{29,30,32,33,42,43} However, Eq. (18) is unsuitable for PIXIE3D-B as it conflicts with the enforcement of the solenoidal property.¹⁸ Instead, we pursue an approach that leverages the divergence cleaning step already performed in PIXIE3D-B (needed due to pollution of the solenoidal property introduced by the preconditioner in the nonlinear iterative solve¹⁴) with minimal additional cost. This is performed as follows:

We begin with the PIXIE3D-B divergence cleaning procedure. PIXIE3D features a cell-centered discretization for the magnetic field,¹⁸ which is not suitable for standard divergence-cleaning procedures employed in staggered meshes.⁴⁵ Instead, PIXIE3D-B solves for the vector potential update for a given a current density update as

$$\nabla \times \nabla \times \delta \mathbf{A} = \nabla \times (\mathbf{B}^{k+1} - \mathbf{B}^k) = \delta \mathbf{J}. \quad (25)$$

Using the Coulomb gauge for the vector potential in this step, we have $\nabla \cdot \mathbf{A} = 0$, and therefore, we can write the divergence-cleaning solution as

$$\nabla^2 \delta \mathbf{A} = -\delta \mathbf{J}. \quad (26)$$

After solving for $\delta \mathbf{A}$, we find that the divergence-cleaned new-time magnetic field is

$$\mathbf{B}^{k+1} = \mathbf{B}^k + \nabla \times \delta \mathbf{A}. \quad (27)$$

In the case of an ideal wall, Eq. (26) is solved with homogeneous Dirichlet BCs for the tangential- \mathbf{A} components (which prevent any flux penetration through the ideal wall) and solenoidal BCs for the normal ones. For a resistive wall, we replace the homogeneous Dirichlet BCs with inhomogeneous ones provided by Eq. (24) as

$$\mathbf{n} \times \delta \mathbf{A}|_a = -\Delta t \mathbf{n} \times \mathbf{E}^k|_a.$$

The new vector potential update found from Eq. (26) with this boundary condition includes the RW response, and it is then used in Eq. (27) to find the new-time magnetic field, which is automatically solenoidal.

3. Implementation in SPECYL

SPECYL can only consider cylindrical geometry, and its RW BC formulation conforms to its spectral nature. The tangential electric field on the wall is specialized using Eq. (17) for non-axisymmetric modes, while the axisymmetric Fourier component is forced to a constant value, to sustain the external loop voltage,

$$\mathbf{E}_a^{0,0} = E_0 \hat{\mathbf{z}}, \quad \mathbf{E}_a^{m,n} = -\frac{a}{\tau_w} \hat{\mathbf{r}} \times [\mathbf{B}_t^{m,n}]_+^- \quad (m, n) \neq (0, 0), \quad (28)$$

where $\hat{\mathbf{r}}$ is the radial unit-vector and all quantities are in Fourier space since SPECYL is a spectral code. Non-axisymmetric tangential magnetic field components are then found by enforcing plasma-wall tangential electric field continuity for each Fourier mode separately,

$$\eta \nabla \times \mathbf{B}_a^{m,n} - \{\mathbf{v} \times \mathbf{B}\}_a^{m,n} = \frac{a}{\tau_w} \hat{\mathbf{r}} \times [\mathbf{B}_t^{m,n}]_+^-, \quad (29)$$

where $\mathbf{B}_a^{m,n} = (\mathbf{B}_r^{m,n} \hat{\mathbf{r}} + \mathbf{B}_t^{m,n})|_{r=a}$, the jump in the tangential magnetic field components in square brackets is computed making use of Eq. (21), and the term in curly brackets is a convolution product between the magnetic field and the edge-plasma velocity over the whole spectrum,

$$\{\mathbf{v} \times \mathbf{B}\}_a^{m,n} = \mathbf{v}_a^{0,0} \times \mathbf{B}_a^{m,n} + \sum_{(p,q) \neq (0,0)} \mathbf{v}_a^{p,q} \times \mathbf{B}_a^{m-p, n-q}.$$

This equation for $\mathbf{B}_a^{m,n}$ is solved semi-implicitly and independently for each mode as

$$\begin{aligned} \eta \nabla \times \mathbf{B}_a^{m,n,k+1} - \mathbf{v}_a^{0,0} \times \mathbf{B}_a^{m,n,k+1} - \frac{a}{\tau_w} \hat{\mathbf{r}} \times [\mathbf{B}_t^{m,n,k+1}]_+^- \\ = \sum_{(p,q) \neq (0,0)} \mathbf{v}_a^{p,q} \times \mathbf{B}_a^{m-p, n-q, k}, \end{aligned}$$

where the superscript k indicates the time level, as before.

TABLE I. General plasma and RW parameters chosen for the RFP and tokamak verification cases are reported in the first and second lines, respectively.

$\alpha(0)$	R	$\eta(0)$	A	B	C	ν	τ_w/τ_A	b/a
4	4	3.33×10^{-5}	20	10	1	10^{-2}	100	1.5
0.5	10	$10^{-5}; 10^{-7a}$	-0.99	2	-1	$= \eta(0)$	$10^{-6} \rightarrow 1^b$	100

^aHere and through the work, we indicate a discrete set of parameter values with semicolons; in this case, either $\eta(0) = 10^{-5}$ or $\eta(0) = 10^{-7}$.

^bHere and throughout this work, we indicate a discrete range of parameter values between two endpoints with an arrow; in this case, τ_w ranges from 10^{-6} to 1.

The normal magnetic field BCs at the resistive wall specialize to the radial component B_r from the general Eq. (18) as

$$(B_r^{0,0})_a = 0, \quad (\partial_r B_r^{m,n})_a = \frac{a}{\tau_w} [\partial_r B_r^{m,n}]_{-}^{+}. \quad (30)$$

Equations (28)–(30) define the general set of RW BCs for SPECYL. Details of their implementation in SPECYL's time-stepping algorithm are given in Appendix A.

B. Flow velocity boundary conditions

It is important to note that magnetic field BCs alone are not sufficient to provide a proper physical description of an RW. Indeed, the presence of normal magnetic field perturbations at the RW, made possible by the magnetic field BCs, must pair with the possibility of normal velocity perturbations. This fact can be understood as a result of the plasma frozen-in law of ideal MHD (which to a good extent holds good in resistive MHD as well, except in the proximity of current sheets) and is an essential feature in particular for free-boundary instabilities such as external kink modes.^{6,46} As a matter of fact, while the magnetic field part of RW boundary

conditions is indeed rather standard as already mentioned in Sec. III A, the self-consistent coupling with flow boundary conditions allowing for a fully 3D velocity field response is still lacking in most of the state-of-the-art MHD codes. Such remarkable self-consistency is demonstrated in this study by the absence of numerically induced boundary layers at the RW regardless of numerical dissipation and proves to be crucial in capturing the physics of external modes in our simplified (circular cross-section, zero- β) model. We further suggest that the proposed 3D flow response is also an essential feature in the description of free-boundary processes under fusion-relevant conditions with MHD codes featuring realistic geometry and physical content.

The flow velocity boundary conditions considered in this study generalize those discussed in Refs. 15 and 19. In such references, the $(\mathbf{E} \times \mathbf{B})$ boundary normal velocity was found from an axisymmetric loop electric field $E_z^{0,0}$, and zero (“no-slip”) boundary conditions were used for the tangential components.

In this study, we consider two generalizations. The first one is to consider a non-axisymmetric loop electric field (and the associated normal flow) with “no-slip” tangential conditions. From the resistive Ohm's law [Eq. (3)] and assuming $\mathbf{v} = v_n \hat{\mathbf{n}}$, we get at the plasma boundary as

$$\mathbf{B} \times [\mathbf{E}_w + v_n \hat{\mathbf{n}} \times \mathbf{B}] = \eta \mathbf{B} \times \mathbf{J} \approx 0,$$

the last statement following from the force-free assumption at the wall. Noting that

$$\mathbf{B} \times (\hat{\mathbf{n}} \times \mathbf{B}) = (|\mathbf{B}|^2 \hat{\mathbf{n}} - B_n \mathbf{B}),$$

we find

$$\hat{\mathbf{n}} \cdot (\mathbf{B} \times \mathbf{E}_w) + v_n |\mathbf{B}_t|^2 = 0,$$

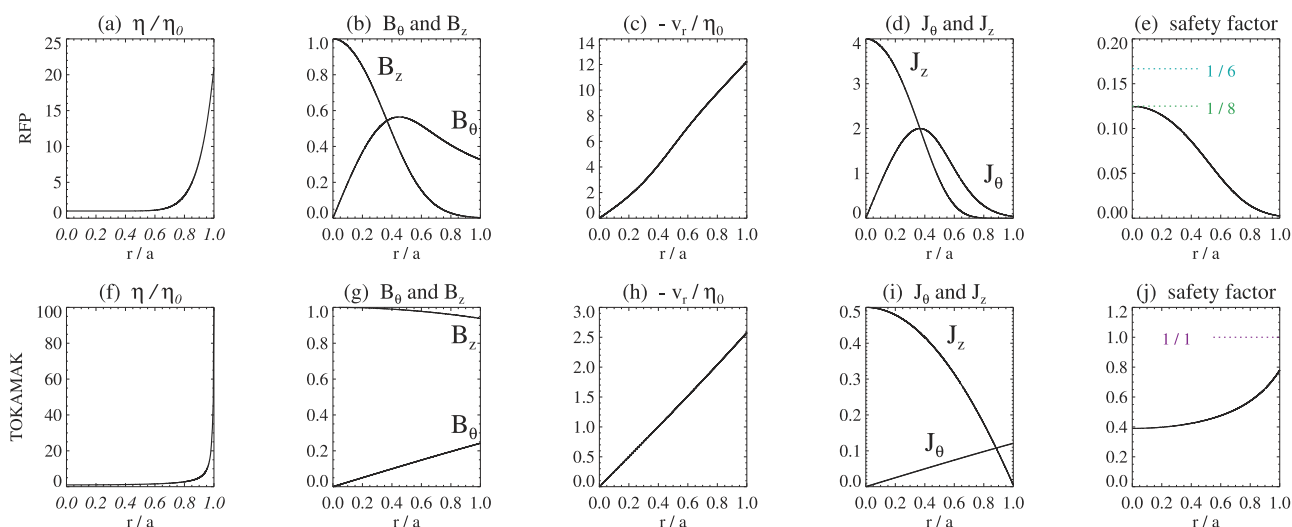


FIG. 2. Initial equilibrium profiles for the simulation cases discussed in Secs. VC 1 and VC 2 (RFP configuration) and Sec. VC 3 (tokamak configuration) are shown in the first and second row, respectively. Radial profiles are reported (from left to right columns) for resistivity normalized to its value on the axis, magnetic field, velocity normalized to resistivity on the axis, current density, and safety factor (with the marked resonances corresponding to the considered MHD modes).

TABLE II. Numeric parameters used in simulations: 2D helical pitch, normalized time-step, and number of points in the radial (N_r) and azimuthal mesh (either number of modes in SPECYL or N_θ in PIXIE3D).

SPECYL					
Nos.	Simulation ID	m/n	$\Delta t/\tau_A$	N_r	N_{modes}^a
1–5	DV_kn0 \rightarrow 4 ^b	1/1	10^{-2}	128	32
6	PP.m1n8.tW1e10	1/8	10^{-3}	100	32
7	PP.m1n8.tW1e2.Vt	1/8	10^{-3}	100	32
8	PP.m1n8.tW1e2.Vp	1/8	10^{-3}	100	32
9–16	PP.m1n6.tW1e2.b/a1 \rightarrow 2	1/6	$10^{-3 \rightarrow -5}$	100	10
17–24	PP.m1n6.tW1e0.b/a1 \rightarrow 2	1/6	$10^{-3 \rightarrow -5}$	100	10
25–29	TK.m1n1.tW1e0 \rightarrow -6.S1e5	1/1	10^{-5}	256	10
30–34	TK.m1n1.tW1e0 \rightarrow -6.S1e7	1/1	10^{-5}	1000	10
35–40	TK.m1n1.tW1e-8.S1e7.qa0.4 \rightarrow 1	1/1	10^{-5}	1000	4
PIXIE3D: versions A and B					
Nos.	Simulation ID	m/n	$\Delta t/\tau_A$	N_r	N_θ
41–45	DV.pixA.kn0 \rightarrow 4	1/1	0.01	128	32
46–50	DV.pixB.kn0 \rightarrow 4	1/1	0.01	128	32
51	PP.m1n8.tW1e10.pixB	1/8	0.1	128	64
52	PP.m1n8.tW1e2.pixA.Vt	1/8	1.0	128	32
53	PP.m1n8.tW1e2.pixA.Vp	1/8	1.0	128	32
54	PP.m1n8.tW1e2.pixB.Vt	1/8	1.0	128	64
55	PP.m1n8.tW1e2.pixB.Vp	1/8	1.0	128	64
56–63	PP.m1n6.tW1e2.pixA.b/a1 \rightarrow 2	1/6	0.01	256	64
64–71	PP.m1n6.tW1e2.pixB.b/a1 \rightarrow 2	1/6	0.01	256	64
72–80	PP.m1n6.tW1e0.pixA.b/a1 \rightarrow 2	1/6	0.01	256	64
81–89	PP.m1n6.tW1e0.pixB.b/a1 \rightarrow 2	1/6	0.01	256	64
90–92	TK.m1n1.tW1e0 \rightarrow -2.S1e5.pixA	1/1	$\tau_w/2N_r$	256	64
93–95	TK.m1n1.tW1e0 \rightarrow -2.S1e7.pixA	1/1	$\tau_w/2N_r$	256	64

^aHere, the number of modes strictly refers to the harmonics with $m > 0$, including their complex-conjugate harmonics with $m < 0$ and the axisymmetric mode. SPECYL simulations consider $2 \times N_{\text{modes}} + 1$ modes, symmetric across (0,0).

^bHere and elsewhere, we use an arrow to condense a group of simulations in one line whose names are diversified only by a numerical value; in this case, these are DV_kn0, DV_kn0.5, DV_kn1, DV_kn2, and DV_kn4.

which gives

$$v_n = \frac{(\mathbf{E}_w \times \mathbf{B}) \cdot \hat{\mathbf{n}}}{|\mathbf{B}_t|^2}, \quad \mathbf{v}_t = 0. \quad (31)$$

This form is implemented verbatim in PIXIE3D. In SPECYL, the spectral representation reads

$$(|\mathbf{B}_t|^2)^{0,0} v_r^{m,n} = \{\mathbf{E}_w \times \mathbf{B} \cdot \hat{\mathbf{r}}\}^{m,n} - \sum_{(p,q) \neq (0,0)} (|\mathbf{B}_t|^2)^{p,q} v_r^{m-p, n-q},$$

which is dealt with in a semi-implicit, serial approach, as in Eq. (29).

In the *vacuum-plasma* interface case ($\tau_w \leq \tau_A$), the plasma boundary is transparent to the magnetic field and it is not appropriate to assume no-slip BCs. Instead, for this specific case, we adopt,

as a second generalization with respect to previous studies, a zero parallel velocity at the edge,

$$v_{\parallel} = 0; \quad \mathbf{v} = \mathbf{v}_{\perp} = \frac{\mathbf{E}_w \times \mathbf{B}}{|\mathbf{B}|^2}. \quad (32)$$

This choice is justified by the fact that the role of parallel velocity in the dynamics of MHD instabilities is typically negligible. Other choices for the parallel velocity component are possible, such as a sheath Bohm-speed boundary condition (as, e.g., in Ref. 38). Unlike Eq. (31), Eq. (32) may feature a normal- \mathbf{E}_w component, which is set to zero in this study. A finite value could, however, be determined by involving additional physics, such as plasma sheath electric fields at the wall. The implementation of the flow BC in the two codes closely mirrors that of Eq. (31). In the following, we will always use Eq. (31) when $\tau_w \gg \tau_A$ (i.e., in the presence of an actual RW) and Eq. (32) when $\tau_w \leq \tau_A$ (i.e., in the case of a plasma-vacuum interface). Note that Eqs. (31) and (32) are equivalent in the linear regime where the normal magnetic field at the boundary is negligible and that they both recover the ideal-wall limit when $B_n \rightarrow 0$ and $\mathbf{E}_w \rightarrow E_z^{0,0} \hat{\mathbf{z}}$.¹⁵

IV. NUMERICAL SETUP

Next, we discuss the numerical setup of the simulations to test the RW boundary condition implementation that was just described. We consider a zero-pressure paramagnetic-pinch axisymmetric equilibrium in cylindrical geometry,^{15,19}

$$\mathbf{J}_0 \times \mathbf{B}_0 = 0, \quad (33)$$

$$\mathbf{E}_0 + \mathbf{v}_0 \times \mathbf{B}_0 = \eta \mathbf{J}_0, \quad (34)$$

with $\mathbf{B} = B_{0,\theta}(r) \hat{\boldsymbol{\theta}} + B_{0,z}(r) \hat{\mathbf{z}}$, $\mathbf{J}_0 = \nabla \times \mathbf{B}_0$, $\mathbf{v}_0 = v_0(r) \hat{\mathbf{r}}$, $\mathbf{E}_0 = E_0 \hat{\mathbf{z}}$, and $\eta = \eta(r)$. The scalar product of Eq. (34) and \mathbf{B}_0 yields

$$\mathbf{J}_0 \cdot \mathbf{B}_0 = \alpha B_{0,z}, \quad \text{with } \alpha(r) \equiv \frac{E_0}{\eta(r)}. \quad (35)$$

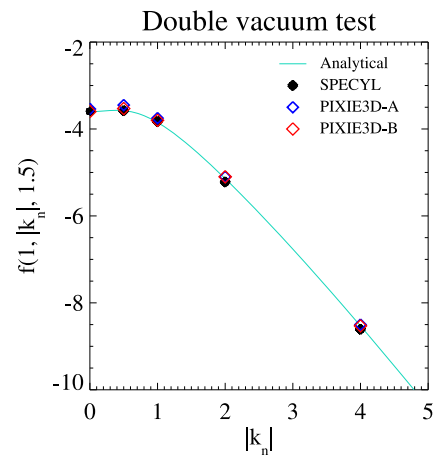


FIG. 3. Comparison of decay rates for the double-vacuum test (with $m = 1$, $b/a = 1.5$).

Equations (33) and (35) along with Faraday’s law imply that $\nabla \times \mathbf{B}_0 = \lambda \mathbf{B}_0$, where the scalar function λ is defined as in Eq. (19) (with $\mathbf{E}_w = E_0 \hat{z}$). We can thus derive two differential equations for $B_{0,\theta}(r)$ and $B_{0,z}(r)$, to be solved iteratively.¹⁹ The resulting relation for the safety factor on the axis is

$$q(0) = \frac{2}{\alpha(0)R}.$$

Finally the (pinch) inward axisymmetric flow velocity results from Ohm’s law [Eq. (34)] are

$$\mathbf{v}_0(r) = -\frac{E_0 B_{0,\theta}}{|\mathbf{B}_0|^2} \hat{\mathbf{r}}. \quad (36)$$

The resistivity profile is parameterized as

$$\eta(r) = \eta(0) \left[1 + A \left(\frac{r}{a} \right)^B \right]^C.$$

The equilibrium parameters for the RFP case-studies are summarized in Table I, which are the same as in Ref. 15. These parameters correspond to the Lundquist number $S = 3 \times 10^4$, viscous Lundquist number $M = 100$, magnetic Prandtl number $P = S/M = 3 \times 10^2$, and Hartmann number $H = \sqrt{SM} = 1.7 \times 10^3$. The equilibrium parameters for the tokamak case are also included in the table. They are chosen to closely approximate the ones used in the theoretical

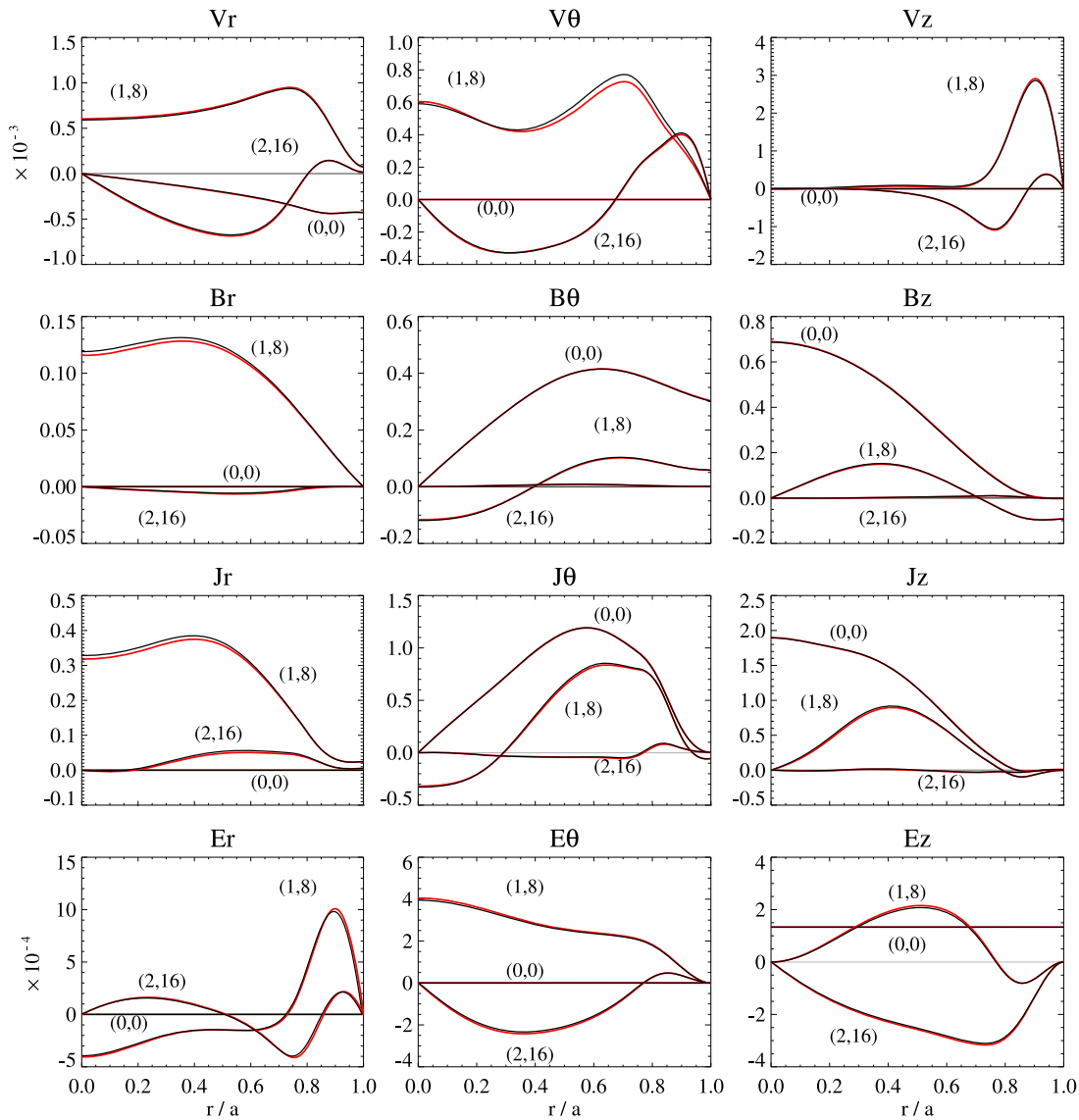


FIG. 4. Radial plots for several plasma quantities of the nonlinearly saturated helical equilibrium after $5000\tau_A$ in the ideal-wall limit ($\tau_w = 10^{10}\tau_A$). Fourier modes $m = 0, 1, 2$ are represented for both PIXIE3D-B (red) and SPECYL (black).

works by Wesson,^{2,46} as will be further discussed at the beginning of Sec. V C 3. Figure 2 displays the corresponding initial equilibrium radial profiles for both RFP and tokamak configurations.

To start the temporal evolution, the equilibrium is perturbed with a small radial-velocity field of the form

$$\delta v_r = \sum_{m,n} \frac{\varepsilon}{r} \sin(\pi r)^{m+2} \cos(m\theta - nz/R),$$

where $\varepsilon = 10^{-6}$ is the perturbation amplitude and the summation runs on the set of perturbed modes. Here, we use $m = 1$ and n as required by the 2D helicity pitch.

All numerical comparisons in our verification study are performed in Fourier space. We consider three main diagnostics:

- Time histories of kinetic and magnetic normalized mode energies:

$$E_{kin}^{m,n} = \int_0^a |\mathbf{v}^{m,n}|^2 r dr, \quad E_{mag}^{m,n} = \int_0^a |\mathbf{B}^{m,n}|^2 r dr.$$

- Radial profiles of \mathbf{v} , \mathbf{B} , \mathbf{J} , and \mathbf{E} components at specified times.

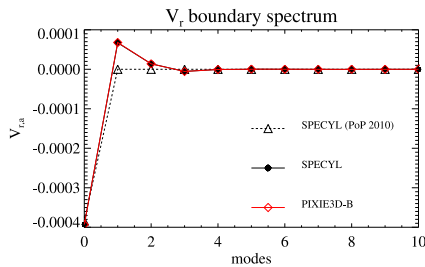


FIG. 5. Spectrum of the radial velocity at the ideal-wall boundary ($\tau_w = 10^{10} \tau_A$) after $5000 \tau_A$ into the simulation. SPECYL (solid black) and PIXIE3D-B (red) are in excellent agreement. The old axisymmetric flow implementation of SPECYL (dashed black) is also reported for reference.

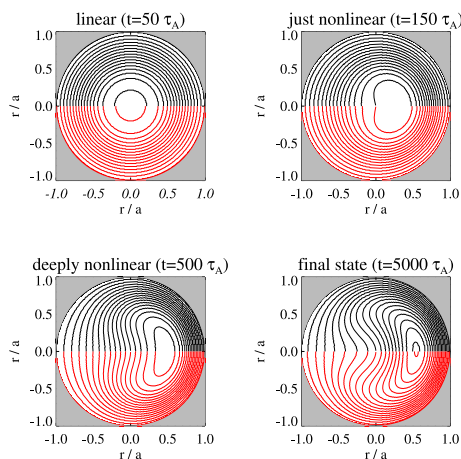


FIG. 6. Evolution of the helical flux in PIXIE3D-B (lower red half) and SPECYL (upper black half) in the ideal-wall limit. Evolution and saturation of the (1, 8) mode are clearly visible. Flux contours do not penetrate the wall in the ideal-wall case.

- Magnetic helical flux $\chi_{m,k_n}(r, u) = mA_z - k_n r A_\theta$, where m and $k_n = n/R$ define the helical pitch and u is the helical angle $u = m\theta - k_n z$.

Table II summarizes the setup and simulation parameters (such as time-step, mesh size for PIXIE3D and number of modes for SPECYL) for the simulations considered in this study. We will consider first a double-vacuum analytical test and then several fusion-relevant cases (RFP and tokamak) with arbitrarily small wall resistivity ($\tau_w = 10^{10}$, which must recover the ideal-wall limit), moderate wall resistivity ($\tau_w = 100$), and large wall resistivity ($\tau_w \leq 1$, which should behave similar to a vacuum interface).

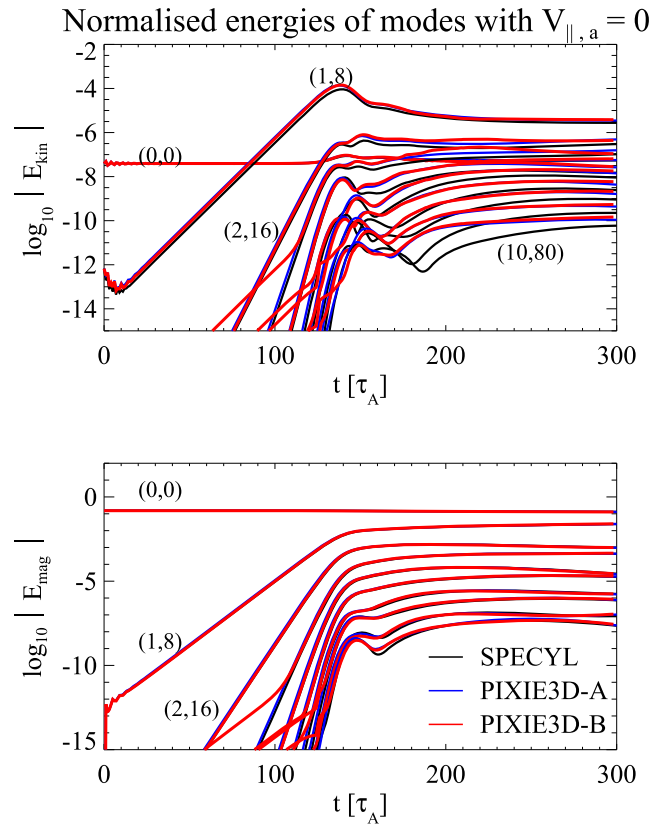


FIG. 7. Time evolution of kinetic and magnetic normalized energies of modes, enforcing $v_{\parallel,a} = 0$ fluid boundary conditions for the nonresonant kink ($m = 1$, $n = 8$) case study. SPECYL (black) and the two implementations of PIXIE3D (blue and red) match well during both linear growth and nonlinear saturation. Early-time disagreements in mode amplitudes for higher (m, n) harmonics in PIXIE3D are caused by numerical pollution from the fundamental mode $m = 1$.

TABLE III. Linear growth rates for the (1, 8) marginally resonant mode.

BCs \ code	specyl	PIXIE3D-A	PIXIE3D-B
$v_{t,a} = 0$	8.751×10^{-2}	8.777×10^{-2}	8.794×10^{-2}
$v_{\parallel,a} = 0$	8.750×10^{-2}	8.777×10^{-2}	8.793×10^{-2}

V. NUMERICAL RESULTS

A. Double-vacuum analytical cylindrical/helical test

We begin the verification study with a test of the RW magnetic field boundary conditions in the limit of negligible plasma response, i.e., with the plasma inside the RW replaced by another vacuum region (hence the name “double-vacuum”). Effective vacuum behavior in the plasma is achieved by setting sufficiently large resistivity and viscosity in the MHD model. Here, we consider $\eta = \nu = 1$ (i.e., $S = M = 1$). Large plasma viscosity will damp any developing flows, isolating the effect of the magnetic field boundary conditions as the main driver of the dynamics.

The solution to the double-vacuum configuration has an analytical solution, which follows the same template as that for the

outer vacuum magnetic field solution. For generic $k_n = n/R \neq 0$, the vacuum solution in the plasma region must be $\mathbf{B} = \nabla\Phi^P$, with the potential amplitudes in Fourier space found by regularity

$$\Phi_{m,n}^P(|k_n|r) = a_m^P(t)I_m(|k_n|r).$$

Here, we have made apparent that the coefficient is time-dependent. The evolution equation for the coefficient is found to be (Appendix D)

$$\frac{\partial_t a_m^P}{a_m^P} = \frac{1}{\tau_w} f(m, |k_n|, b). \tag{37}$$

The right hand side of this equation is given explicitly in Eqs. (D1) and (D2) in Appendix D and can be shown to be negative-definite.

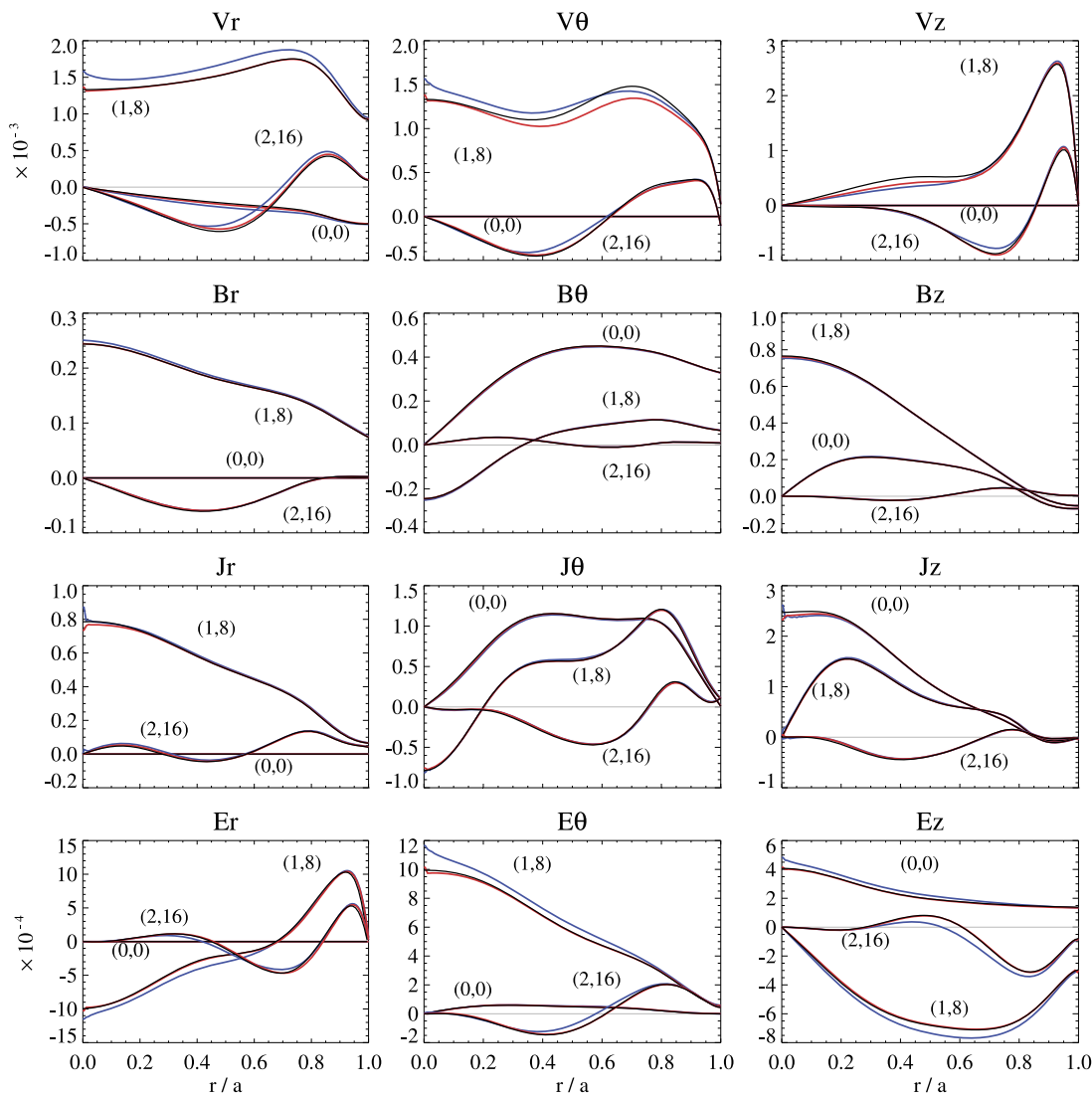


FIG. 8. Radial plot of the main plasma quantities, after $300\tau_A$ from initial perturbation (1, 8), with $\tau_w/\tau_A = 100$ and enforcing $v_{\parallel,a} = 0$. Fourier modes $m = 1, 2, 3$ represent SPECTYL (black), PIXIE3D-A (blue), and PIXIE3D-B (red).

11 September 2023 14:44:00

Therefore, the double-vacuum solution decays exponentially at a rate dependent on m , k_n , b , and τ_w .

Figure 3 illustrates the excellent agreement between numerical and analytical decay rates for the double-vacuum problem for $m = 1$ and $b/a = 1.5$. Markers correspond to simulations: referring to Table II, simulations No. 1–No. 5 are for SPECYL and No. 41–No. 45 and No. 46–No. 50 are for PIXIE3D-A and PIXIE3D-B, respectively. Other setup parameters are taken as indicated in Table I. In each simulation, the decay rate is fitted numerically and divided by τ_w ; different values of τ_w have been explored, giving consistent results.

B. Ideal-wall verification in the limit $\tau_w \rightarrow \infty$

In this test, we explore the ideal-wall limit case by taking $\tau_w = 10^{10} \tau_A$ in simulation No. 6 for SPECYL and No. 51 for PIXIE3D-B (refer to Table II for simulation parameters). In this limit, we expect no magnetic field penetration of the wall (i.e., $B_r \approx 0$ at the wall) so that no-slip ($\mathbf{v}_t = 0$) occurs and $v_{\parallel} = 0$ fluid BCs are equivalent. Hence, we just consider a single version of PIXIE3D with no-slip BCs, as previously specified at the end of Sec. III B.

The case study is a marginally resonant (on axis) kink mode ($m = 1, n = 8$) in RFP geometry using the equilibrium described in Sec. IV. Throughout this work, we adopt the convention that positive m and n correspond to a helical pitch consistent with that of field lines in the plasma core. Figure 4 displays the radial, azimuthal, and axial components of the first three Fourier modes of several relevant plasma quantities at $5000\tau_A$ when a nonlinear helical equilibrium is reached.

Figure 4 is equivalent to Fig. 10 of Ref. 15 but is obtained as a limit case of our RW BC treatment. In the reference mentioned above, SPECYL adopted a purely axisymmetric pinch velocity at plasma edge, which the proposed BCs successfully generalize to a full-spectrum edge-flow, which is in perfect agreement with PIXIE3D (as shown in greater detail in Fig. 5).

Figure 6 presents the helical flux function on a cylindrical cross section $z = 0$ for both codes at selected times. As already visible in Fig. 4, outcomes of the two codes are very similar: the progress in the radial displacement of the helical axis from the center is almost identically reproduced. Note that flux contours do not penetrate the ideal wall, as expected.

Measured numerical growth rates for the $(1, -8)$ mode are $\gamma\tau_A = 7.797 \times 10^{-2}$ for SPECYL and $\gamma\tau_A = 7.821 \times 10^{-2}$ for PIXIE3D, which agree within 0.3%. This simulation will be the base case for the verification of our resistive-wall implementation.

C. Thin resistive shell verification study

We focus next on the principal aim of this nonlinear verification study, that is, the effect of a wall with finite resistivity on the MHD dynamics. We will consider three different scenarios for our 2D helical geometry verification study of the thin-shell resistive implementation in SPECYL and PIXIE3D: a marginally resonant $(1, 8)$ kink mode in the RFP (the same as that considered in Ref. 15), a non-resonant $(1, 6)$ mode in the RFP, and an external $(1, 1)$ kink mode in a tokamak.

1. Marginally resonant $(1, 8)$ kink mode in the RFP

Simulations considered here are No. 7 and No. 8 for SPECYL and No. 52 and No. 53 and No. 54 and No. 55 for the two versions of PIXIE3D, respectively (refer to Table II). For this first case study, we looked into both fluid BCs for completeness even if no-slip BCs are more appropriate in the presence of a physical RW ($\tau_w = 100\tau_A$).

Figure 7 reports the time evolution of the kinetic and magnetic energies of the first 11 modes, including the axisymmetric one, under $v_{\parallel,a} = 0$ BCs. The same plot enforcing no-slip BCs (not shown) yields no visible change compared to Fig. 7 in this specific case. SPECYL (in black) and both versions of PIXIE3D (blue and red) match quite well for both kinetic energies and magnetic energies.

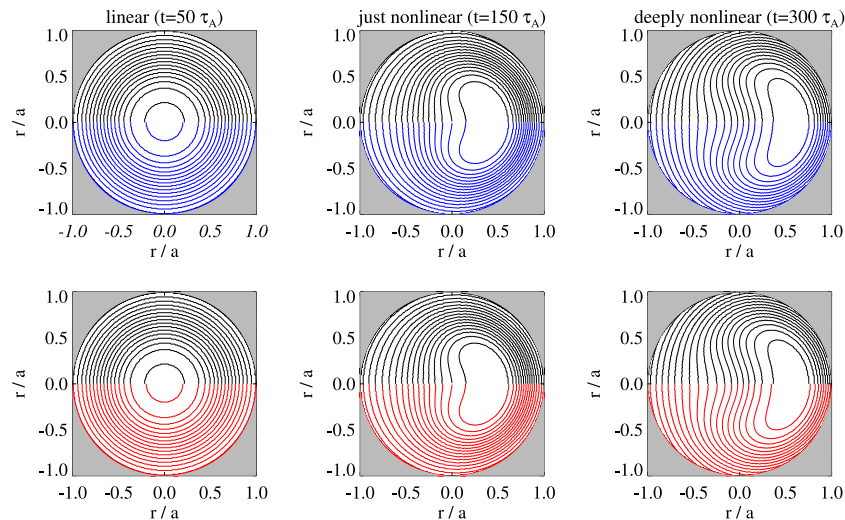


FIG. 9. Evolution of the helical flux projection on the cylindrical cross section for PIXIE3D-A (blue), PIXIE3D-B (red), and SPECYL (black). Faster growth and dominance of mode $m = 1$ with respect to Fig. 6 and field penetration on the RW time-scale are visible.

The linear growth rates are reported in Table III, which agree with each other within 0.2%. The nonlinear saturation agrees quite well in all panels. Figure 8 reports the radial profiles of plasma quantities after $300\tau_A$ of evolution from initial perturbation for SPECYL (black), PIXIE3D-A (blue) and PIXIE3D-B (red), enforcing $v_{\parallel,a} = 0$. Once more, the similarity is remarkable overall, with minor differences that at any rate do not involve the boundary region and are of the same magnitude as those reported in Ref. 15 for the ideal wall case.

Finally, Fig. 9 compares the evolution of the helical flux from both SPECYL and PIXIE3D, following the usual colormap convention. Agreement is excellent, with both codes showing the emergence and dominance of mode $m = 1$. Magnetic field penetration through the wall is apparent on timescales longer than the RW time-constant τ_w (panels in the second and third column).

2. Nonresonant (1, 6) kink mode in the RFP

We consider the non-resonant (1, 6) mode on the same RFP equilibrium as the previous case to study its stability with respect to the variation in the ideal wall proximity to the edge of the plasma. Simulations involved in this scan are No. 9–No. 24 for SPECYL, No. 56–No. 63 and No. 72–No. 80 for PIXIE3D-A, and No. 64–No. 71 and No. 81–No. 89 for PIXIE3D-B.

Two different RW penetration time-scales have been examined: $\tau_w = 100\tau_A$ (a resistive thin shell with no-slip BCs) and $\tau_w = \tau_A$ (a vacuum-wall with $v_{\parallel,a} = 0$). Figure 10 presents the growth-rate scan on the separation of the ideal wall from the plasma for both RW configurations. For each simulation, the growth rate is reported.

When the ideal wall is attached to the plasma, the kink mode (1, 6) is linearly stable ($\gamma\tau_A \approx -5.37 \times 10^{-3}$ with SPECYL and

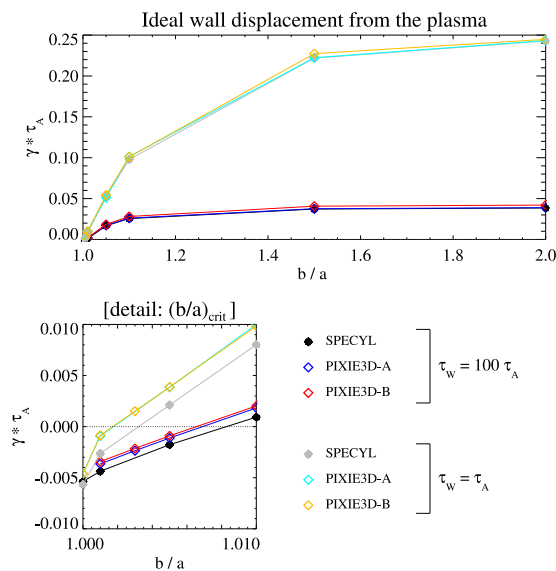


FIG. 10. Linear growth rate of the nonresonant mode (1, 6) in RFP geometry as a function of ideal wall proximity and for two different values of τ_w , from SPECYL (black and gray dots), PIXIE3D-A (blue and cyan diamonds), and PIXIE3D-B (red and orange diamonds). For the vacuum-wall limit case ($\tau_w = \tau_A$), $v_{\parallel,a} = 0$ BCs are used. The detail highlights the marginal stability thresholds in b/a from all codes.

$\gamma\tau_A \approx -4.7 \times 10^{-3}$ with both versions of PIXIE3D). As the ideal wall separates, the growth rate increases up to a marginal stability threshold $(b/a)_{\text{crit}}$ that depends on the value of τ_w . This is highlighted in the side-panel (Fig. 10-bottom), with the details of stability threshold crossing. It is apparent that the larger the value of τ_w , the slower the increase in the growth rate. Both codes find similar linear instability thresholds: $(b/a)_{\text{crit}} \approx 1.003$ in SPECYL and $(b/a)_{\text{crit}} \approx 1.002$ with both versions of PIXIE3D for $\tau_w = \tau_A$ and $(b/a)_{\text{crit}} \approx 1.007$ for $\tau_w = 100\tau_A$ for all codes. Overall, the comparison shows excellent agreement between the two codes, particularly away from the stability threshold when the growth rates saturate as the stabilizing effect of the ideal wall becomes negligible due to its distance from the plasma.

3. External (1, 1) kink mode in the tokamak

The last case study we present is a (1, 1) external kink mode in tokamak geometry. For the numerical setup, refer to Table II (simulations No. 25–No. 34 for SPECYL, and simulations No. 90–No. 95 for PIXIE3D-A). In particular, $\tau_w \leq \tau_A$ and $v_{\parallel} = 0$ are enforced to produce the free plasma–vacuum interface.

The initial equilibrium parameters for the tokamak case are provided in the second line of Table I and approximately correspond to the ones used in the theoretical studies by Wesson.^{2,46} The corresponding equilibrium profiles are depicted in Figs. 2(f)–2(j). The very low edge value of the safety factor ($q_a < 1$) is motivated by the requirement that the (1, 1) mode is an external kink mode. Although such a configuration is typically avoided in fusion plasmas due to its high disruptivity, it is of interest for its intrinsically high Ohmic heating and because it can be experimentally reproduced with a proper MHD control.⁴⁷ Moreover, the analysis presented in this section is also relevant to the (2, 1) external kink mode in the configuration with an edge safety factor $q_a < 2$, which is more accessible and appealing from the experimental point of view.⁴⁸

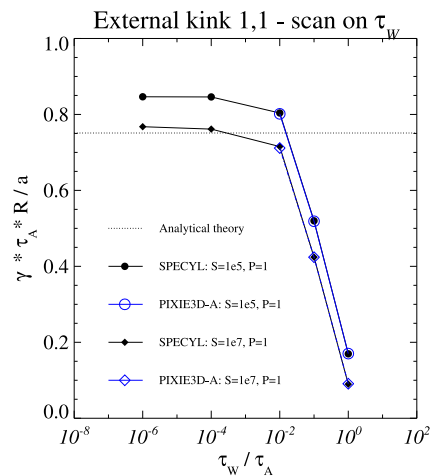


FIG. 11. Growth rate of the external kink (1, 1) in tokamak geometry as a function of τ_w for $q_a \approx 0.78$. PIXIE3D-A (blue circles and diamonds) and SPECYL (black dots and diamonds) agree well for the same numerical setup. SPECYL recovers the expected growth-rate γ_{exp} [Eq. (38)] for sufficiently small η , ν , and τ_w ($\tau_w \ll 1/\gamma_{\text{exp}}$).

Figure 11 again demonstrates excellent agreement between SPECYL and PIXIE3D-A (within 0.3% for $S = 10^5$ and 1% for $S = 10^7$) for the tokamak case in the limit of large aspect ratios ($R/a = 10$) and small τ_w . For such small τ_w values, PIXIE3D's time step [which is determined by the time step stability limit in Eq. (22)] is quite small for the radial resolutions considered. For this reason, we have not considered τ_w values below 0.01 in PIXIE3D-A, and we have not included simulations with PIXIE3D-B (which is significantly more expensive than PIXIE3D-A in these regimes due to the divergence-cleaning solution required per time step). SPECYL's spectral treatment is much faster as it can consider only a few Fourier modes for the linear study, allowing the exploration of much smaller τ_w values.

In the figure, we compare the linear growth rates γ found in simulations for different input values of $\tau_w \leq \tau_A$; a strong inverse dependence between them is evident for $\tau_w > 0.01\tau_A$, followed by asymptotic saturation for faster penetration scales. A milder direct dependence of γ with the plasma resistivity and viscosity is also observed.

An analytical prediction of the expected growth rate can be found from the ideal MHD energy principle in the large aspect-ratio tokamak limit,² which defines a variational principle to find the most energetically favorable plasma-shape relaxation displacement $\xi = \sum_{m,n} \xi^{m,n}(r)e^{im\theta - ik_n z - i\omega t}$ with

$$\omega^2 = \frac{-\frac{1}{2}W(\xi)}{\int_V dV \frac{\rho}{2} |\xi|^2}, \quad W(\xi) = \int_V dV [J(\xi) \times \mathbf{B}(\xi) - \nabla p(\xi)] \cdot \xi^*,$$

where $V = V_{\text{plasma}} + V_{\text{vacuum}}$ is the volume of the whole system, ξ^* is the complex-conjugate of ξ , and the work W produced in the relaxation is treated as a cost function, whose minimum defines the energetically favorable displacement. The linear instability growth rate $\gamma_{\text{exp}} = -\text{Im}(\omega)$ is either positive or null. For the large aspect ratio limit, ∇p gives a negligible contribution, and for the $m = 1$ kink mode, an analytical prediction of the linear instability growth rate is given as a function of the edge-value of the safety factor and of the plasma aspect ratio,⁴⁶

$$\begin{cases} \left(\frac{\gamma_{\text{exp}} \tau_A R}{a}\right)^2 = \frac{2}{q_a^2} (1 - q_a) q_a, & \text{if } q_a \leq 1, \\ \gamma_{\text{exp}} = 0, & \text{if } q_a > 1. \end{cases} \quad (38)$$

The expected growth rate for the case study shown in Fig. 11 is also reported as a dotted horizontal line. Remarkably, numerical simulations with our 3D-flow boundary conditions approximate γ_{exp} to be increasingly well for increasingly ideal plasma conditions (decreasing $\eta(0)$ and ν , thus increasing S and M) and for $\tau_w \ll 1/\gamma_{\text{exp}}$.

Figure 12 presents the radial velocity during the linear growth, normalized to its value on the axis, for SPECYL and PIXIE3D-A, for the case of $\eta(0) = \nu = 10^{-5}$, $\tau_w = 10^{-2}\tau_A$, and after $\tau_w = 100\tau_A$ from the initial perturbation. The analytical theory predicts a uniform radial flow ($v_r^{1,1}/v_{r,0}^{1,1} = \xi_r^{1,1}/\xi_{r,0}^{1,1}$), which is also reported for comparison. The figure shows excellent agreement between linear theory and both codes, except for a small boundary layer at plasma edge, which gradually disappears as τ_w decreases.

Figure 13 presents a scan performed with the SPECYL code on the edge-value of the safety-factor using a larger aspect ratio

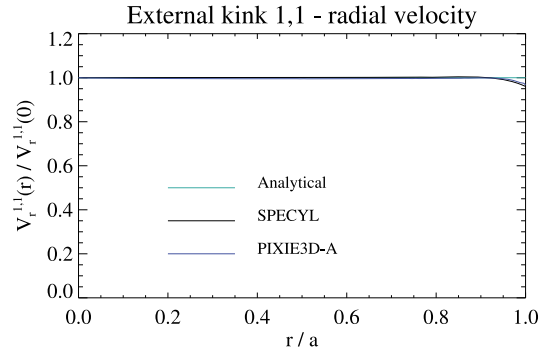


FIG. 12. Normalized radial velocity during the linear growth for $q_a \approx 0.78$, $\eta(0) = \nu = 10^{-5}$ and $\tau_w = 10^{-2}\tau_A$ and after $100\tau_A$ from initial perturbation. The analytical expectation is very well matched by both codes; the small discrepancy at plasma edge becomes increasingly negligibly as τ_w is decreased.

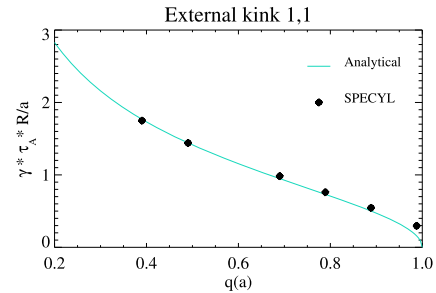


FIG. 13. Linear benchmark of SPECYL's simulations against the ideal MHD external kink mode (1, 1). Slight disagreement around $q(a) \approx 1$ is due to resistive modes resonating at the plasma edge. For this case, $R/a = 20$, $\tau_w/\tau_A = 10^{-8}$, and $\eta(0) = \nu = 10^{-7}$.

($R/a = 20$) for numerical stability of the most unstable modes ($q_a \leq 0.5$) since γ_{exp} scales with the inverse aspect-ratio [see Eq. (38)]. SPECYL's simulations used as shown in this figure are reported in Table II as No. 35–No. 40. Other setup parameters in Fig. 13 are $\tau_w = 10^{-8}\tau_A$, $\nu = \eta(0) = 10^{-7}$, $N_{\text{modes}} = 4$, $N_r = 10^3$, and $\Delta t = 10^{-5}$, as reported also in Table II. The analytical prediction is very well reproduced except for $q_a \approx 1$, at which point the competing resonant MHD phenomena (e.g., tearing modes) at the plasma edge can interfere with the growth rate measurement.

VI. CONCLUSIONS AND FINAL REMARKS

The successful verification of numerical codes is a prerequisite for reliability. The present work comes as a substantial extension of a previous and successful verification¹⁵ between the nonlinear 3D MHD codes SPECYL and PIXIE3D, featuring now a more realistic thin-shell formulation of the plasma boundary. This is a flexible setup capable of reproducing various physical regimes by adjusting the resistive penetration time of the shell τ_w , from an ideal wall attached to the plasma edge ($\tau_w \gg \tau_A$) to a free interface with vacuum ($\tau_w \leq \tau_A$). The intermediate case ($\tau_w > \tau_A$, but still smaller than the target simulation time) represents a finite-conductivity shell separating the plasma from a vacuum region and from an outer ideal wall. The position of the outer ideal wall, i.e., the so-called shell

proximity b/a , is also tunable. This makes it possible to study the instability threshold for external kink modes.

In this study, we have derived the RW model equations in general curvilinear coordinates, later specialized to cylindrical/helical, and described three alternative implementations: SPECYL, PIXIE3D-A, and PIXIE3D-B, which we have verified thoroughly against each another. Our only assumption in the derivation is that the inertial and viscous effects can be neglected at the plasma boundary. Such an assumption could however be relaxed for future studies, if needed. Two alternative BC implementations have been considered for the boundary flow: an $\mathbf{E} \times \mathbf{B}$ drift normal to the boundary, $v_{t,a} = 0$, used when the interface is meant to represent a physical shell and no parallel flow to the magnetic field, $v_{||,a} = 0$, used to model the free-interface case. A quick overview of the implementations of the RW module in SPECYL, PIXIE3D-A, and PIXIE3D-B has been provided, as well as differences in the approaches resulting from structural differences between the codes.

Overall, the numerical verification exercise has demonstrated excellent agreement between SPECYL and PIXIE3D across all the considered physical problems. Our verification began with two limiting cases that disentangle the magnetic and fluid boundary treatments: the double-vacuum case and the ideal-wall limit. In the double-vacuum case study, the linear decay of an initially stimulated magnetic signal is measured and compared to its analytical expectation. In this case, no plasma flow develops, and the dynamics are mainly driven by the magnetic-field RW BCs. In the ideal wall case, no field penetration through the shell is allowed, and a pinch flow develops due to the presence of a loop voltage.

Subsequently, we considered three different scenarios in 2D (helical) geometry: the nonlinear evolution of a marginally resonant $(m, n) = (1, 8)$ kink mode and of a non-resonant $(1, 6)$ kink mode in the RFP configuration and the linear stability of the external kink mode $(1, 1)$ in the tokamak. In the first case, featuring a kink mode that is already unstable in the presence of an ideal wall in contact with the plasma, overall excellent agreement is found between SPECYL and both formulations of PIXIE3D, both enforcing no-slip and $v_{||,a} = 0$ fluid boundary conditions. The substantial agreement found on relatively long, highly nonlinear simulations is evidence of a robust consistency between the codes.

The stability of the nonresonant $(1, 6)$ kink mode has been investigated for diverse ideal wall proximities and for the two relevant cases of a resistive shell attached to the plasma and of a free-interface with vacuum. This is an external kink mode that becomes unstable when the ideal wall is moved away from the plasma. The good agreement between SPECYL and PIXIE3D is confirmed also in this case, both regarding the linear growth rates and the instability threshold beyond the critical plasma-wall proximity ratio.

The $(1, 1)$ tokamak case is the most challenging of the three due to the smallness of τ_w , η , and ν considered. Excellent agreement is found between SPECYL and PIXIE3D in their common range of application, in both growth rates and the theoretically expected eigenfunction profiles. Both codes find a strong dependence of the mode growth rate on the vacuum-wall penetration time and a milder dependence on the plasma resistivity and viscosity. Moreover, for wall penetration times much shorter than the inverse growth rate, and for an almost ideal plasma, excellent agreement with the analytical ideal MHD growth rate prediction is found.

The present study confirms the mathematical correctness of both codes after the implementation of the magneto-fluid set of RW boundary conditions and opens the path for their application to relevant physical problems. For the RFP, a preliminary 3D application of RW magnetic field boundary conditions with SPECYL, assuming a purely normal and axisymmetric velocity boundary (no flow RW BCs), was reported in Ref. 49. A similar study will be carried out in the future using the full set of RW BCs described in this paper to confirm and extend the validity of the results obtained there, with the aim of providing predictions about the MHD dynamics in the future device RFX-mod2.^{49–51} Another topic of interest for the RFP community is the question of how realistically wall boundary conditions affect the emergence of helical RFP states.^{5,52–58} Preliminary 3D SPECYL simulations with RFX-mod-like equilibrium parameters, again using the above-mentioned approximations,^{59,60} showed that RW BCs can foster the spontaneous emergence of $m = 1, n = 7$ helical states similar to RFX-mod experiments. This quite promising observation motivates an extended study using the full RW BCs documented here and will be the subject of a future study. The two research lines outlined above for the RFP will also benefit from a further planned modification of the RW BCs in SPECYL. A second resistive shell will be included between the existing one and the ideal wall, separated from each by tunable-width vacuum regions. A large resistivity will be typically assumed for the wall at the plasma boundary, consistent, for instance, with the carbon tiles in contact with the plasma in RFX-mod, while the second wall at a finite distance from the plasma will represent the true conducting shell. This setup is already implemented in the axisymmetric-flow BC version of SPECYL and is currently being generalized to the case with fully self-consistent 3D boundary flow. Such modification will enable the study of instabilities such as the resistive wall mode, for which a vacuum gap between the plasma and RW is required. For the tokamak, future PIXIE3D studies will focus on the generalization of the vacuum magnetic-field response to toroidal geometries to enable the study of vertical displacement events and resistive-wall modes in realistic ITER configurations. PIXIE3D is already capable of modeling disruptions in ITER-like geometries with scrape-off layers including strongly varying, temperature dependent resistivity and strong parallel conductivity anisotropy.⁶¹ The documented RW module treatment, which is in general geometry and is motivated by sound physics principles related to continuity of the tangential electric field components at the wall and consistency with Ohm's law, is expected to work seamlessly with current and future PIXIE3D's physics capabilities.

ACKNOWLEDGMENTS

This work could not be possible without the generous financial support of Los Alamos National Laboratory and the University of Padova for a month-long visit of L.S. at LANL in the summer of 2022. In addition, Consorzio RFX provided for the open-access publication fee. L.C. was funded by the Applied Mathematics Research Program of the Department of Energy Office of Applied Scientific Computing Research and the TDS project of the Scientific Discovery from the Advanced Computation (SciDAC) DOE Fusion-Energy-Sciences/Applied-Scientific-Computing-Research Partnership Program. L.C.'s research was performed under the auspices of the National Nuclear Security Administration of the U.S. Department

of Energy at Los Alamos National Laboratory, managed by Triad National Security, LLC, under Contract No. 89233218CNA000001. L.C. used computing resources provided by the Los Alamos National Laboratory Institutional Computing Program. This work has been carried out within the framework of the EUROfusion Consortium, funded by the European Union via the Euratom Research and Training Program (Grant Agreement No 101052200—EUROfusion). Views and opinions expressed are, however, those of the authors only and do not necessarily reflect those of the European Union or the European Commission. Neither the European Union nor the European Commission can be held responsible for them.

AUTHOR DECLARATIONS

Conflict of Interest

The authors have no conflicts to disclose.

Author Contributions

L. Spinicci: Conceptualization (equal); Data curation (equal); Formal analysis (equal); Funding acquisition (equal); Investigation (equal); Methodology (equal); Project administration (equal); Resources (equal); Software (equal); Visualization (equal); Writing – original draft (equal); Writing – review & editing (equal). **D. Bonfiglio:** Conceptualization (equal); Formal analysis (equal); Investigation (equal); Methodology (equal); Project administration (equal); Resources (equal); Software (equal); Supervision (equal); Validation (equal); Writing – review & editing (lead). **L. Chacón:** Conceptualization (equal); Data curation (equal); Formal analysis (equal); Funding acquisition (equal); Investigation (equal); Methodology (equal); Project administration (equal); Resources (equal); Software (equal); Supervision (equal); Validation (equal); Writing – original draft (equal); Writing – review & editing (equal). **S. Cappello:** Resources (equal); Software (equal); Supervision (equal); Validation (equal); Writing – review & editing (equal). **M. Veranda:** Resources (equal); Software (equal); Writing – review & editing (equal).

DATA AVAILABILITY

The data that support the findings of this study are available from the corresponding author upon reasonable request.

APPENDIX A: TIME-STEPPING IN THE SPECYL CODE

We summarize the scheme of the SPECYL main temporal loop, a simplified version of which is reported in Fig. 14. The code evolves the magnetic field and the flow velocity, along with the current density, over time according to a predictor-corrector scheme.

The predictor semi-step advances the fields from the preceding time step t_n to some fraction of the simulation time resolution Δt (usually, $t^* = t^n + 0.5 \cdot \Delta t$). At this time level, resistivity is neglected, and the predicted \mathbf{B}_t^* is obtained for each mode via the ideal Ohm's law:

$$\frac{\mathbf{B}_t^* - \mathbf{B}_t^n}{t^* - t^n} = -\nabla \times (\mathbf{v}^n \times \mathbf{B}^n).$$

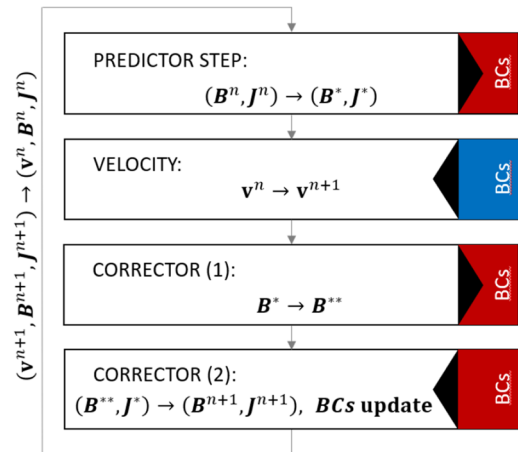


FIG. 14. Workflow of the main loop of SPECYL: the magnetic field, the flow, and the current-density are updated through a predictor-corrector scheme. Magnetic BCs (red) are enforced several times, while fluid BCs (blue) are enforced only once. A black triangle marks the direction of the radial solution of the equation within each step: the predictor and the first part of the corrector step are explicitly solved from the axis to the edge; the velocity step and the second part of the corrector step proceed semi-implicitly from the edge to the axis.

The radial component results from the solenoidal property $\nabla \cdot \mathbf{B}^* = 0$. The predicted current is also computed for later use,

$$\mathbf{J}^* = \nabla \times \mathbf{B}^*.$$

The solution of the above-mentioned equations is explicit and proceeds from the axis outward, with the outermost values of \mathbf{B}_t^* modes being assigned through the BCs while $B_{r,a}^*$ is kept at its prior value.

The velocity update to time $t^{n+1} = t^n + \Delta t$ leverages the momentum balance equation [Eq. (1)] with predicted fields \mathbf{B}^* and \mathbf{J}^* , integrating from the edge to the axis: this way, the fluid BCs, which were computed at the end of the prior iteration of the main loop, penetrate the plasma domain.

The corrector step integrates Ampère's and Faraday's law [Eqs. (2)–(4)] for the full time-step from t^n to t^{n+1} ,

$$\frac{\mathbf{B}^{n+1} - \mathbf{B}^n}{\Delta t} = \nabla \times \left[\left(\frac{\mathbf{v}^{n+1} + \mathbf{v}^n}{2} \right) \times \mathbf{B}^* \right] - \nabla \times (\eta \nabla \times \mathbf{B}^{n+1}).$$

However, this is broken into two simpler computations using an intermediate magnetic field \mathbf{B}^{**} . The first part of the corrector step solves for the tangential component from

$$\frac{\mathbf{B}_t^{**} - \mathbf{B}_t^n}{\Delta t} = \nabla \times \left[\left(\frac{\mathbf{v}^{n+1} + \mathbf{v}^n}{2} \right) \times \mathbf{B}^* \right],$$

with the radial- \mathbf{B}^{**} component derived from $\nabla \cdot \mathbf{B}^{**} = 0$. This is another explicit update, where BCs only influence $\mathbf{B}_{t,a}^{**}$ modes while $B_{r,a}^{**}$ is kept constant. The second part of the corrector completes the step,

$$\frac{\mathbf{B}^{n+1} - \mathbf{B}^{**}}{\Delta t} = -(\nabla \eta) \times (\nabla \times \mathbf{B}^{n+1}) + \eta \nabla^2 \mathbf{B}^{n+1}. \quad (\text{A1})$$

This time, all the components of the magnetic field are updated simultaneously with the BCs computed from Eqs. (29) and (30), as described in the next section. Integration proceeds from the edge to the axis. Field BCs are then used to produce flow velocity BCs, as discussed in Sec. III B, to be enforced in the velocity step of the subsequent time step. A final divergence cleaning step is then enforced on B_r^{n+1} . As in the two previous divergence cleaning steps, this is performed for each harmonic separately, through the numerical integration of B_r from the axis to the wall using the equation $\partial_r(rB_r) = -\partial_\theta B_\theta - r\partial_z B_z$ and leaving $B_r(a)$ unchanged. In this way, the error in the divergence of \mathbf{B}^{n+1} for each Fourier mode is kept at a machine-precision level. At the end of this procedure, the current density is recomputed from Ampère's law as

$$\mathbf{J}^{n+1} = \nabla \times \mathbf{B}^{n+1}.$$

APPENDIX B: NORMAL-B RESISTIVE-WALL EVOLUTION EQUATION IN GENERAL CURVILINEAR COORDINATES

In this section, we derive the evolution equation for the normal component of the magnetic field in generalized curvilinear geometry. We begin from Eq. (18),

$$\partial_t(\mathbf{n} \cdot \mathbf{B})_a + \frac{a}{\tau_w} \nabla \cdot [|\mathbf{n}| \delta \mathbf{B}_t]_a = 0. \quad (\text{B1})$$

Writing the divergence in curvilinear geometry,

$$\partial_t(B_a^n) + \frac{a}{\tau_w} \sum_{i \neq n} \partial_i (|\mathbf{n}| B^i)_a^\pm = 0, \quad (\text{B2})$$

where $B^i = \mathbf{J} \mathbf{B} \cdot \nabla \xi_i$, $\mathbf{n} = \nabla \xi_n$, and J is the Jacobian of $\mathbf{x}(\xi)$. Using the solenoidal property of the magnetic field, $\partial_i B^i = 0$, we can further write

$$\begin{aligned} \sum_{i \neq n} \partial_i (|\mathbf{n}| B^i)_a^\pm &= \sum_{i \neq n} [|\mathbf{n}| \partial_i (B^i)_a^\pm + B^i|_a^\pm \partial_i |\mathbf{n}|_a] \\ &= -|\mathbf{n}| (\partial_n B^n)_a^\pm + \sum_{i \neq n} (B^i)_a^\pm \partial_i |\mathbf{n}|_a. \end{aligned}$$

Consequently,

$$\partial_t(B_a^n) - \frac{a|\mathbf{n}|}{\tau_w} (\partial_n B^n)_a^\pm + \frac{a}{\tau_w} \sum_{i \neq n} (B^i)_a^\pm \partial_i |\mathbf{n}|_a = 0,$$

where the last term takes care of the non-orthogonality of the coordinate transformation at the wall. Note that $\partial_{i \neq n} |\mathbf{n}| = 0$ for orthogonal coordinate systems. Otherwise,

$$\partial_i |\mathbf{n}| = (\partial_i \mathbf{n}) \cdot \frac{\mathbf{n}}{|\mathbf{n}|} = -\frac{1}{J|\mathbf{n}|} \Gamma_{ij}^n g^{jn},$$

where $\Gamma_{ij}^n = -(\nabla \mathbf{n})_{ij}$ is the Christoffel symbol of the second kind. Therefore, the final evolution equation for the normal component is

$$\partial_t(B_a^n) - \frac{a|\mathbf{n}|}{\tau_w} (\partial_n B^n)_a^\pm - \frac{a}{\tau_w} \frac{1}{J|\mathbf{n}|} \sum_{i \neq n} (B^i)_a^\pm \Gamma_{ij}^n g^{jn} = 0. \quad (\text{B3})$$

For cylindrical/helical geometry at $r = a$, this equation specializes to the well-known one,⁶²

$$\partial_t B_{r,a} = \frac{a}{\tau_w} [\partial_r B_r]_a^\pm, \quad (\text{B4})$$

which is reported in Eq. (30).

APPENDIX C: RW VACUUM RESPONSE IN CYLINDRICAL/HELICAL GEOMETRY

We seek to compute the vacuum tangential magnetic field components (just outside the cylindrical RW) from the normal component B_n , which is continuous across the RW and therefore determined by the plasma (thin-shell approximation).

By definition, in vacuum, there are no charge-carriers so that $\mathbf{J} = \mathbf{0}$. This implies irrotationality for the vacuum magnetic field via Faraday's law, i.e., $\mathbf{B} = \nabla \Phi$. We can define

$$\Phi_{m,n}(r, \theta, z) = \phi_{m,n}(r) e^{im\theta + ik_n z} \quad (\text{C1})$$

such that for each Fourier mode,

$$\{\mathbf{B}^{m,n}\}^V = \nabla \Phi_{m,n}.$$

The axisymmetric mode of Eq. (C1) possibly includes a linear gauge function of periodic variables θ and z ; this term has no relevance for the RW treatment, and we drop it for simplicity. Let us now consider a vacuum domain bound by the RW at $r = a$ and an ideally conducting wall at $r = b > a$. Hence,

$$\partial_r \Phi_{m,n}|_{r=a} = B_{r,a}^{m,n}; \quad \partial_r \Phi_{m,n}|_{r=b} = 0, \quad (\text{C2})$$

where $B_{r,a}^{m,n} = B_r^{m,n}|_{r=a}$. The solenoidal property becomes

$$\nabla^2 \Phi_{m,n} = 0, \quad (\text{C3})$$

which for cylindrical coordinates reads

$$\frac{1}{r} \partial_r (r \partial_r \Phi_{m,n}) - \left[\frac{m^2}{r^2} + k_n^2 \right] \Phi_{m,n} = 0.$$

We can now discuss three cases:

1. General: $\forall m$ and $k_n \neq 0$

The solutions to this equation are modified Bessel functions of the first and second kind, $I_m(|k_n|r)$ and $K_m(|k_n|r)$, and hence,

$$\Phi_{m,n}(r) = \mathfrak{A} I_m(|k_n|r) + \mathfrak{B} K_m(|k_n|r).$$

Coefficients \mathfrak{A} and \mathfrak{B} are determined from (C2),

$$\begin{aligned} \mathfrak{A} |k_n| I'_m(|k_n|a) + \mathfrak{B} |k_n| K'_m(|k_n|a) &= B_{r,a}^{m,n}, \\ \mathfrak{A} |k_n| I'_m(|k_n|b) + \mathfrak{B} |k_n| K'_m(|k_n|b) &= 0. \end{aligned}$$

Here, $B_{r,a}^{m,n}$ are the Fourier amplitudes of the normal component of the magnetic field at the plasma wall. Solving for \mathfrak{A} and \mathfrak{B} , we find

$$\Phi_{m,n}(r, b) = B_{r,a}^{m,n} g_{m,n}(r, b), \quad (\text{C4})$$

where

$$g_{m,n}(r, b) = \frac{1}{|k_n|} \left[\frac{I'_m(|k_n|b)K_m(|k_n|r) - K'_m(|k_n|b)I_m(|k_n|r)}{I'_m(|k_n|b)K'_m(|k_n|a) - K'_m(|k_n|b)I'_m(|k_n|a)} \right]. \quad (C5)$$

We now can find the components of the magnetic field at the outside of the RW from

$$\{B_r^{m,n}\}^V|_{r=a} = \partial_r \Phi_{m,n}|_{r=a} = B_{r,a}^{m,n}, \quad (C6)$$

$$\{B_\theta^{m,n}\}^V|_{r=a} = \frac{1}{r} \partial_\theta \Phi_{m,n}|_{r=a} = \frac{im}{a} B_{r,a}^{m,n} g_{n,m}(a, b), \quad (C7)$$

$$\{B_z^{m,n}\}^V|_{r=a} = \partial_z \Phi|_{r=a} = ik_n B_{r,a}^{m,n} g_{n,m}(a, b), \quad (C8)$$

where $g_{m,n}(a, b)$ is found from Eq. (C5). Thus, ultimately, the tangential magnetic field Fourier components relative to the normal ones are given by

$$\left\{ \frac{B_\theta^{m,n}}{i B_r^{m,n}} \right\}_{r=a}^V = m g_{m,n}(a, b) \equiv \Theta_{m,n}(a, b), \quad (C9)$$

$$\left\{ \frac{B_z^{m,n}}{i B_r^{m,n}} \right\}_{r=a}^V = k_n g_{m,n}(a, b) \equiv Z_{m,n}(a, b). \quad (C10)$$

This result is reported in Eq. (21).

2. Large aspect ratio (or $n = 0$): $m \neq 0$ and $k_n = 0$

In this case, Eq. (C3) has a simple polynomial solution,

$$\Phi_{m,n} = \mathfrak{A} r^m + \mathfrak{B} r^{-m}.$$

Enforcing the same boundary conditions Eq. (C2) yields

$$\Phi_{m,0}(r) = B_{r,a}^{m,0} \cdot g_{m,0}(r, b),$$

where

$$g_{m,0}(r, b) = \frac{a}{m} \frac{(b/a)^m}{1 - (b/a)^{2m}} \left[\left(\frac{r}{b}\right)^m + \left(\frac{b}{r}\right)^m \right].$$

Equations (C9) and (C10) specialize to

$$\left\{ \frac{B_\theta^{m,0}}{i B_r^{m,0}} \right\}_{r=a}^V = m g_{m,0}(a, b) = \Theta_{m,0}(a, b),$$

$$\left\{ \frac{B_z^{m,0}}{i B_r^{m,0}} \right\}_{r=a}^V = 0 = Z_{m,n}(a, b).$$

3. Axisymmetric mode: $m = k_n = 0$

This case is best analyzed by solving the original equation,

$$\frac{1}{r} \partial_r (r \partial_r \Phi_{0,0}) = 0.$$

Integrating over the vacuum region,

$$\int_a^b r dr \frac{1}{r} \partial_r (r \partial_r \Phi_{0,0}) = 0 \Rightarrow b \partial_r \Phi_{0,0}|_{r=b} = a \partial_r \Phi_{0,0}|_{r=a}.$$

However, since $B_n(b) = \partial_r \Phi_{0,0}|_{r=b} = 0$ at the perfect conductor region, this implies $\partial_r \Phi_{0,0}|_{r=a} = 0$, i.e., no penetration, consistent with the previous ideal wall implementation.

The axisymmetric part of the vacuum magnetic field can, however, retain an azimuthal component $\{B_\theta\}^V \sim 1/r$ and a uniform axial component $\{B_z\}^V$. Such components do not explicitly enter the RW implementation of either code and are related to the magnetic fields produced by the plasma current and by the external solenoidal coils, respectively.

APPENDIX D: DOUBLE-VACUUM ANALYTICAL SOLUTION IN A CYLINDER

The vacuum solution inside the plasma is obtained analytically in a similar manner to the solution in the outside vacuum region, i.e., Fourier-analyzing and solving the resulting differential equation per mode. Because generic $k_n = n/R \neq 0$, the vacuum solution in the plasma region must be by regularity,

$$\Phi_{m,n}^P(|k_n|r) = a_m^P(t) I_m(|k_n|r),$$

where we have made apparent that the coefficient is time dependent (in fact, decaying). The corresponding initial condition for the magnetic field in the plasma region is [with $a^P(t=0) = 1$]

$$\{B_r^{m,n}\}^P = \partial_r \Phi_{m,n}^P = a_m^P(t) |k_n| I'_m(|k_n|r),$$

$$\{B_\theta^{m,n}\}^P = \partial_\theta \Phi_{m,n}^P = a_m^P(t) im I_m(|k_n|r),$$

$$\{B_z^{m,n}\}^P = \partial_z \Phi_{m,n}^P = 0.$$

The vacuum solution beyond the RW, by continuity of the normal derivative (normal component of the magnetic field), is found from Eq. (C4),

$$\{B_r^{m,n}\}^V = \partial_r \Phi_{m,n} = a_m^P(t) |k_n| I'_m(|k_n|a) g'_{m,n}(r, b).$$

We seek an analytical solution for the temporal evolution of the coefficient $a_m^P(t)$. This is found from Eq. (B4), giving

$$\frac{\partial_t a_m^P}{a_m^P} = \frac{1}{\tau_w} \left[g''_{m,n}(a, b) - |k_n| \frac{I''_m(|k_n|a)}{I'_m(|k_n|a)} \right] = \frac{1}{\tau_w} f(m, |k_n|, b), \quad (D1)$$

where

$$g''_{m,n}(a, b) = |k_n| \frac{I'_m(|k_n|b)K''_m(|k_n|a) - K'_m(|k_n|b)I''_m(|k_n|a)}{I'_m(|k_n|b)K'_m(|k_n|a) - K'_m(|k_n|b)I'_m(|k_n|a)}.$$

The case of $k_n = 0$ (large aspect ratio, or $n = 0$) has

$$\Phi_{m,0}^P(r) = a_m^P(t) r^m,$$

$$\Phi_{m,0}^V(r) = a_m^P(t) m a^{m-1} g_{m,0}(r, b),$$

$$g_{m,0}(r, b) = \frac{a}{m} \frac{(b/a)^m}{1 - (b/a)^{2m}} \left[\left(\frac{r}{b}\right)^m + \left(\frac{b}{r}\right)^m \right],$$

and thus,

$$\{B_1^{m,n}\}^P = \partial_1 \Phi_{m,n}^P = a_m^P(t) m r^{m-1},$$

$$\{B_1^{m,n}\}^V = a_m^P(t) m a^{m-1} g'_{m,0}(r, b).$$

Equation (D1) then reduces to

$$\frac{\partial a_m^p}{\partial t} = -\frac{1}{\tau_w} \frac{2}{a} \frac{(b/a)^{2m}}{(b/a)^{2m} - 1} = \frac{1}{\tau_w} f(m, 0, b). \quad (\text{D2})$$

In both Eqs. (D1) and (D2), the r.h.s. is negative and does not depend on time. Hence, our analysis predicts exponential decay.

REFERENCES

- ¹W. M. Tang, “Advanced computations in plasma physics,” *Phys. Plasmas* **9**, 1856 (2002).
- ²J. A. Wesson, *Tokamaks*, 3rd ed. (Oxford University Press, 2004), Chap. 6.
- ³M. Wakatani, *Stellarator and Heliotron Devices* (Oxford University Press, 1998).
- ⁴D. F. Escande, P. H. Diamonds, X. Garbet, P. Ghendrih, and Y. Sarazin, “What is a reversed field pinch?” in *Rotation and Momentum Transport in Magnetized Plasmas* (World Scientific, 2014), pp. 247–286, Chap. 6.
- ⁵L. Marrelli, P. Martin, M. E. Puiatti, J. S. Sarff, B. Chapman, J. R. Drake, D. F. Escande, and S. Masamune, “The reversed field pinch,” *Nucl. Fusion* **61**, 023001 (2021).
- ⁶J. P. Freidberg, *Ideal MHD* (Cambridge University Press, 2014), p. 11, Chap. 8.
- ⁷R. Fitzpatrick, *Plasma Physics: An Introduction*, 2nd ed. (CRC Press, Boca Raton, FL, 2022), Chap. 3 and 5.
- ⁸J. P. Freidberg, *Plasma Physics and Fusion Energy* (Cambridge University Press, 2014).
- ⁹P. Piovesan *et al.*, “Role of a continuous MHD dynamo in the formation of 3D equilibria in fusion plasmas,” *Nucl. Fusion* **57**, 076014 (2017).
- ¹⁰Ü. Stroth, D. Aguiar, E. Alessi, C. Angioni, N. Arden, R. A. Parra, V. Artigues, O. Asunta, M. Balden, V. Bandaru, A. Banon-Navarro, K. Behler, A. Bergmann, M. Bergmann, J. Bernardo, M. Bernert, A. Biancalani, R. Bielajew, R. Bilato, G. Birkenmeier, T. Blanken, V. Bobkov, A. Bock, T. Body, T. Bolzonella, N. Bonanomi, A. Bortolon, B. Bösowirth, C. Bottereau, A. Bottino, H. van den Brand, M. Brenzke, S. Brezinsek, D. Brida, F. Brochard, C. Bruhn, J. Buchanan, A. Bühler, A. Burckhart, Y. Camenen, B. Cannas, P. C. Megias, D. Carlton, M. Carr, P. Carvalho, C. Castaldo, M. Cavedon, C. Cazzaniga, C. Challis, A. Chanin, C. Cianfarani, F. Claret, S. Coda, R. Coelho, J. Coenen, L. Colas, G. Conway, S. Costea, D. Coster, T. Cote, A. Creely, G. Croci, D. C. Zabala, G. Cseh, A. Czarnecka, I. Cziegler, O. D’Arcangelo, A. D. Molin, P. David, C. Day, M. de Baar, P. de Marné, R. Delogu, S. Denk, P. Denner, A. Di Siena, J. D. Palacios Durán, D. Dunai, A. Drenik, M. Dreval, R. Drube, M. Dunne, B. Duval, R. Dux, T. Eich, S. Elgeti, A. Encheva, K. Engelhardt, B. Erdős, I. Erofeev, B. Esposito, E. Fable, M. Faitsch, U. Fantz, M. Farnik, H. Faugel, F. Felici, O. Ficker, S. Fietz, A. Figueredo, R. Fischer, O. Ford, L. Frassinetti, M. Fröschle, G. Fuchert, J. Fuchs, H. Fünfgelder, S. Futatani, K. Galazka, J. Galdon-Quiroga, D. G. Escolà, A. Gallo, Y. Gao, S. Garavaglia, M. G. Muñoz, B. Geiger, L. Giannone, S. Gibson, L. Gil, E. Giovannozzi, S. Glöggler, M. Gobbin, J. G. Martin, T. Goodman, G. Gorini, T. Görler, D. Gradic, G. Granucci, A. Gräter, H. Greuner, M. Griener, M. Groth, A. Gude, L. Guimarais, S. Günter, G. Haas, A. Hakola, C. Ham, T. Happel, N. den Harder, G. Harrer, J. Harrison, V. Hauer, T. Hayward-Schneider, B. Heinemann, T. Hellsten, S. Henderson, P. Hennequin, A. Herrmann, E. Heyn, F. Hitzler, J. Hübner, K. Höfler, J. Holm, M. Hölzl, C. Hopf, L. Horvath, T. Höschen, A. Houben, A. Hubbard, A. Huber, K. Hunger, V. Igochine, M. Iliasova, T. Ilkei, K. I. Björk, C. Ionita-Schrittewieser, I. Ivanova-Stanik, W. Jacob, N. Jaksic, F. Janky, A. Jansen van Vuuren, A. Jardin, F. Jaulmes, F. Jenko, T. Jensen, E. Joffrin, A. Kallenbach, S. Kálvin, M. Kantor, A. Kappatou, O. Kardaun, J. Karhunen, C. P. Käsemann, S. Kasilov, A. Kendl, W. Kernbichler, E. Khilkévitch, A. Kirk, S. K. Hansen, V. Klevarova, G. Kocsis, M. Koleva, M. Komm, M. Kong, A. Krämer-Flecken, K. Krieger, A. Krivska, O. Kudlacek, T. Kurki-Suonio, B. Kurzan, B. Labit, K. Lackner, F. Lagner, A. Lahtinen, P. Lang, P. Lauber, N. Leuthold, L. Li, J. Likonon, O. Linder, B. Lipschultz, Y. Liu, A. Lohs, Z. Lu, T. Luda di Cortemiglia, N. Luhmann, T. Lunt, A. Lysoivan, T. Maceina, J. Madsen, A. Magnanimo, H. Maier, J. Mailloux, R. Maingi, O. Maj, E. Maljaars, P. Manas, A. Mancini, A. Manhard, P. Mantica, M. Mantsinen, P. Manz, M. Maraschek, C. Marchetto, L. Marrelli, P. Martin, A. Martitsch, F. Matos, M. Mayer, M. L. Mayoral, D. Mazon, P. McCarthy, R. McDermott, R. Merkel, A. Merle, D. Meshcheriakov, H. Meyer, D. Milanesio, P. M. Cabrera, F. Monaco, M. Muraca, F. Nabais, V. Naulin, R. Nazikian, R. Nem, A. Nemes-Czopf, G. Neu, R. Neu, A. Nielsen, S. Nielsen, T. Nishizawa, M. Nocente, J. M. Noterdaeme, I. Novikau, S. Nowak, M. Oberkofler, R. Ochoukov, J. Olsen, F. Orain, F. Palermo, O. Pan, G. Papp, I. P. Perez, A. Pau, G. Pautasso, C. Paz-Soldan, P. Petersson, P. Piovesan, C. Piron, U. Plank, B. Plaum, B. Plöck, V. Plyusnin, G. Pokol, E. Poli, L. Porte, T. Pütterich, M. Ramisch, J. Rasmussen, G. Ratta, S. Ratynskaia, G. Raupp, D. Réfy, M. Reich, F. Reimold, D. Reiser, M. Reisner, D. Reiter, T. Ribeiro, R. Riedl, J. Riesch, D. Rittich, J. R. Rodriguez, G. Rocchi, P. Rodriguez-Fernandez, M. Rodriguez-Ramos, V. Rohde, G. Ronchi, A. Ross, M. Rott, M. Rubel, D. Ryan, F. Ryter, S. Saarelma, M. Salewski, A. Salmi, O. Samoylov, L. S. Sanchez, J. Santos, O. Sauter, G. Schall, K. Schlüter, K. Schmid, O. Schmitz, P. Schneider, R. Schrittwieser, M. Schubert, C. Schuster, T. Schwarz-Selinger, J. Schweinzer, E. Seliunin, A. Shabbir, A. Shalpegin, S. Sharapov, U. Sheikh, A. Shevelev, G. Sias, M. Siccino, B. Sieglin, A. Sigalov, A. Silva, C. Silva, D. Silvagni, J. Simpson, S. Sipilä, E. Smigelskis, A. Snicker, E. Solano, C. Sommariva, C. Sozzi, G. Spizzo, M. Spolaore, A. Stegmeier, M. Stejner, J. Stober, E. Strumberge, G. S. Lopez, H. J. Sun, W. Suttröpp, E. Sytova, T. Szepesi, B. Täl, T. Tala, G. Tardini, M. Tardocchi, D. Terranova, M. Teschke, E. Thorén, W. Tierens, D. Told, W. Treutterer, G. Trevisan, E. Trier, M. Tripsky, M. Usovltceva, M. Valisa, M. Valovic, M. van Zeeland, F. Vannini, B. Vanovac, P. Varela, S. Varoutis, N. Vianello, J. Vicente, G. Verdoolaege, T. Vierle, E. Viezzer, I. Voitsekhoivitch, U. von Toussaint, D. Wagner, X. Wang, M. Weiland, A. White, M. Willensdorfer, B. Winger, M. Wischmeier, R. Wolf, E. Wolfrum, Q. Yang, Q. Yu, R. Zagórski, I. Zammuto, T. Zehetbauer, W. Zhang, W. Zholobenko, M. Zilker, A. Zito, H. Zohm, S. Zoletnik EUROfusion MST1 Team, “Progress from ASDEX upgrade experiments in preparing the physics basis of ITER operation and DEMO scenario development,” *Nucl. Fusion* **62**, 042006 (2022).
- ¹¹M. Siccino, W. Biel, E. Fable, T. Franke, F. Janky, P. Lang, M. Mattei, F. Maviglia, F. Palermo, O. Sauter, M. Tran, S. Van Mulders, and H. Zohm, “Impact of the plasma operation on the technical requirements in EU-DEMO,” *Fusion Eng. Des.* **179**, 113123 (2022).
- ¹²M. Greenwald, “Verification and validation for magnetic fusion,” *Phys. Plasmas* **17**, 058101 (2010).
- ¹³S. Cappelletto and D. Biskamp, “Reconnection processes and scaling laws in reversed field pinch magnetohydrodynamics,” *Nucl. Fusion* **36**, 571 (1996).
- ¹⁴L. Chacón, “An optimal, parallel, fully implicit Newton–Krylov solver for three-dimensional viscoresistive magnetohydrodynamics,” *Phys. Plasmas* **15**, 056103 (2008).
- ¹⁵D. Bonfiglio, L. Chacón, and S. Cappelletto, “Nonlinear three-dimensional verification of the SPECYL and PIXIE3D magnetohydrodynamics codes for fusion plasmas,” *Phys. Plasmas* **17**, 082501 (2010).
- ¹⁶A. Kryzhanovskyy, D. Bonfiglio, S. Cappelletto, M. Veranda, and M. Zuin, “Alfvén waves in reversed-field pinch and tokamak ohmic plasmas: Nonlinear 3D MHD modeling and comparison with RFX-mod,” *Nucl. Fusion* **62**, 086019 (2022).
- ¹⁷D. S. Harned and W. Kerner, “Semi-implicit method for three-dimensional compressible magnetohydrodynamic simulation,” *J. Comput. Phys.* **60**, 62–75 (1985).
- ¹⁸L. Chacón, “A non-staggered, conservative, $\nabla \cdot \vec{B} = 0$ finite-volume scheme for 3D implicit extended magnetohydrodynamics in curvilinear geometries,” *Comput. Phys. Commun.* **163**, 143–171 (2004).
- ¹⁹G. L. Delzanno, L. Chacón, and J. M. Finn, “Electrostatic mode associated with the pinch velocity in reversed field pinch simulations,” *Phys. Plasmas* **15**, 122102 (2008).
- ²⁰D. Biskamp, *Nonlinear Magnetohydrodynamics* (Cambridge University Press, 1993), Chap. 9.
- ²¹F. Auriemma, R. Lorenzini, M. Agostini, L. Carraro, G. D. Masi, A. Fassina, M. Gobbin, E. Martines, P. Innocente, P. Scarin, W. Schneider, and M. Zuin, “Characterization of particle confinement properties in RFX-mod at a high plasma current,” *Nucl. Fusion* **55**, 043010 (2015).
- ²²L. Chacón and D. A. Knoll, “A fully implicit 3D extended magnetohydrodynamics algorithm,” in *33rd EPS Conference Proceedings* (Curran Associates, Inc., 2006), Vol. 30I, pp. 1–164.
- ²³C. Gimblett, “On free boundary instabilities induced by a resistive wall,” *Nucl. Fusion* **26**, 617 (1986).
- ²⁴T. Hender, C. Gimblett, and D. Robinson, “Effects of a resistive wall on magnetohydrodynamic instabilities,” *Nucl. Fusion* **29**, 1279 (1989).

- ²⁵M. G. Haines, C. G. Gimblett, and R. J. Hastie, "Intrinsic rotation due to MHD activity in a tokamak with a resistive wall," *Plasma Phys. Controlled Fusion* **55**, 055002 (2013).
- ²⁶J. M. Finn and C. R. Sovinec, "Nonlinear tearing modes in the presence of resistive wall and rotation," *Phys. Plasmas* **5**, 461–480 (1998).
- ²⁷E. A. Saad and P. R. Brunzell, "Experimental characterization and modelling of the resistive wall mode response in a reversed field pinch," *Plasma Phys. Controlled Fusion* **64**, 055011 (2022).
- ²⁸V. D. Pustovitov, "General formulation of the resistive wall mode coupling equations," *Phys. Plasmas* **15**, 072501 (2008).
- ²⁹D. Schnack and S. Ortolani, "Computational modelling of the effect of a resistive shell on the RFX reversed field pinch experiment," *Nucl. Fusion* **30**, 277 (1990).
- ³⁰R. Paccagnella, D. Terranova, and P. Zanca, "Modelling and interpretation of MHD active control experiments in RFX-mod," *Nucl. Fusion* **47**, 990–996 (2007).
- ³¹Y. L. Ho and S. C. Prager, "Nonlinear reversed-field pinch dynamics with nonideal boundaries," *Phys. Fluids B* **3**, 3099–3110 (1991).
- ³²A. Marx and H. Lütjens, "Free-boundary simulations with the XTOR-2F code," *Plasma Phys. Controlled Fusion* **59**, 064009 (2017).
- ³³H. Strauss, A. Pletzer, W. Park, S. Jardin, J. Breslau, and L. Sugiyama, "MHD simulations with resistive wall and magnetic separatrix," *Comput. Phys. Commun.* **164**, 40–45 (2004), proceedings of the 18th International Conference on the Numerical Simulation of Plasmas.
- ³⁴N. M. Ferraro, S. C. Jardin, L. L. Lao, M. S. Shephard, and F. Zhang, "Multi-region approach to free-boundary three-dimensional tokamak equilibria and resistive wall instabilities," *Phys. Plasmas* **23**, 056114 (2016).
- ³⁵P. Merkel and E. Strumberger, "Linear MHD stability studies with the STARWALL code," [arXiv:1508.04911](https://arxiv.org/abs/1508.04911) [physics.plasm-ph] (2015).
- ³⁶M. Hölzl, P. Merkel, G. T. A. Huysmans, E. Nardon, E. Strumberger, R. McAdams, I. Chapman, S. Günter, and K. Lackner, "Coupling JOEKE and STARWALL codes for non-linear resistive-wall simulations," *J. Phys.: Conf. Ser.* **401**, 012010 (2012).
- ³⁷M. Hoelzl, G. T. A. Huysmans, P. Merkel, C. Atanasiu, K. Lackner, E. Nardon, K. Aleynikova, F. Liu, E. Strumberger, R. McAdams, I. Chapman, and A. Fil, "Non-linear simulations of MHD instabilities in tokamaks including eddy current effects and perspectives for the extension to halo currents," *J. Phys.: Conf. Ser.* **561**, 012011 (2014).
- ³⁸F. J. Artola, A. Loarte, E. Matveeva, J. Havlicek, T. Markovic, J. Adamek, J. Cavalier, L. Kripner, G. T. A. Huysmans, M. Lehnen, M. Hoelzl, and R. Panek, "Simulations of COMPASS vertical displacement events with a self-consistent model for halo currents including neutrals and sheath boundary conditions," *Plasma Phys. Controlled Fusion* **63**, 064004 (2021).
- ³⁹F. J. Artola, C. R. Sovinec, S. C. Jardin, M. Hoelzl, I. Krebs, and C. Clauser, "3D simulations of vertical displacement events in tokamaks: A benchmark of M3D-C¹, NIMROD, and JOEKE," *Phys. Plasmas* **28**, 052511 (2021).
- ⁴⁰M. Bonotto, Y. Q. Liu, F. Villone, L. Pigatto, and P. Bettini, "Expanded capabilities of the CarMa code in modeling resistive wall mode dynamics with 3-D conductors," *Plasma Phys. Controlled Fusion* **62**, 045016 (2020).
- ⁴¹V. Igochine, S. Günter, K. Lackner, and E. Strumberger, "Error field amplification in the presence of a resistive wall," in *31st EPS Conference on Plasma Physics* (Proceedings of Science, 2004), Vol. 28G, p. 4.129.
- ⁴²S. E. Kruger, C. R. Sovinec, D. D. Schnack, and E. D. Held, "Free-boundary simulations of DIII-D plasmas with the NIMROD code," *Comput. Phys. Commun.* **164**, 34–39 (2004).
- ⁴³A. L. Becerra, "Resistive wall and error field studies using the extended MHD code NIMROD," M.Sc. thesis (University of Wisconsin – Madison, 2016), https://cptc.wisc.edu/wp-content/uploads/sites/327/2017/09/UW-CPTC_17-2.pdf.
- ⁴⁴K. J. Bunkers and C. R. Sovinec, "The influence of boundary and edge-plasma modeling in computations of axisymmetric vertical displacement," *Phys. Plasmas* **27**, 112505 (2020).
- ⁴⁵J. U. Brackbill and D. C. Barnes, "The effect of nonzero $\nabla \cdot \mathbf{B}$ on the numerical solution of the magnetohydrodynamic equations," *J. Comput. Phys.* **35**, 426–430 (1980).
- ⁴⁶J. Wesson, "Hydromagnetic stability of tokamaks," *Nucl. Fusion* **18**, 87 (1978).
- ⁴⁷N. C. Hurst, B. E. Chapman, A. F. Almagri, B. S. Cornille, S. Z. Kubala, K. J. McCollam, J. S. Sarff, C. R. Sovinec, J. K. Anderson, D. J. Den Hartog, C. B. Forest, M. D. Pandya, and W. S. Solsrud, "Self-organized magnetic equilibria in tokamak plasmas with very low edge safety factor," *Phys. Plasmas* **29**, 080704 (2022).
- ⁴⁸C. Piron, P. Martin, D. Bonfiglio, J. Hanson, N. Logan, C. Paz-Soldan, P. Piovesan, F. Turco, J. Bialek, P. Franz, G. Jackson, M. Lanctot, G. Navratil, M. Okabayashi, E. Strait, D. Terranova, and A. Turnbull, "Interaction of external $n = 1$ magnetic fields with the sawtooth instability in low- q RFX-mod and DIII-D tokamaks," *Nucl. Fusion* **56**, 106012 (2016).
- ⁴⁹L. Marrelli, R. Cavazzana, D. Bonfiglio, M. Gobbin, G. Marchiori, S. Peruzzo, M. E. Puiatti, G. Spizzo, D. Voltolina, P. Zanca, M. Zuin, G. Berton, P. Bettini, T. Bolzonella, A. Canton, S. Cappello, L. Carraro, L. Cordaro, S. Dal Bello, M. Dalla Palma, G. De Masi, A. Fassina, F. Gnesotto, L. Grando, P. Innocente, F. Lunardon, G. Manduchi, D. Marcuzzi, N. Marconato, R. Piovano, N. Pomaro, A. Rigoni, A. Rizzolo, P. Scarin, M. Siragusa, P. Sonato, S. Spagnolo, M. Spolaore, and D. Terranova, "Upgrades of the RFX-mod reversed field pinch and expected scenario improvements," *Nucl. Fusion* **59**, 076027 (2019).
- ⁵⁰S. Peruzzo, M. Agostini, P. Agostinetti, M. Bernardi, P. Bettini, T. Bolzonella, A. Canton, L. Carraro, R. Cavazzana, S. Dal Bello, M. Dalla Palma, G. De Masi, R. Delogu, A. Fassina, L. Grando, P. Innocente, G. Marchiori, N. Marconato, L. Marrelli, N. Patel, M. E. Puiatti, P. Scarin, M. Siragusa, P. Sonato, M. Spolaore, L. Trevisan, M. Valisa, M. Vallar, P. Vincenzi, A. Zamengo, P. Zanca, and L. Zanotto, "Design concepts of machine upgrades for the RFX-mod experiment," *Fusion Eng. Des.* **123**, 59–62 (2017), proceedings of the 29th Symposium on Fusion Technology (SOFT-29) Prague, Czech Republic, September 5-9, 2016.
- ⁵¹S. Peruzzo, M. Bernardi, R. Cavazzana, S. Dal Bello, M. Dalla Palma, L. Grando, E. Perin, R. Piovano, A. Rizzolo, F. Rossetto, D. Ruardo, M. Siragusa, P. Sonato, and L. Trevisan, "Detailed design of the RFX-mod2 machine load assembly," *Fusion Eng. Des.* **136**, 1605–1613 (2018), Special Issue: Proceedings of the 13th International Symposium on Fusion Nuclear Technology (ISFNT-13).
- ⁵²R. Lorenzini, E. Martines, P. Piovesan, D. Terranova, P. Zanca, M. Zuin, A. Alfier, D. Bonfiglio, F. Bonomo, A. Canton, S. Cappello, L. Carraro, R. Cavazzana, D. F. Escande, A. Fassina, P. Franz, M. Gobbin, P. Innocente, L. Marrelli, R. Pasqualotto, M. E. Puiatti, M. Spolaore, M. Valisa, N. Vianello, and P. Martin, "Self-organized helical equilibria as a new paradigm for ohmically heated fusion plasmas," *Nat. Phys.* **5**, 570–574 (2009).
- ⁵³D. Terranova, A. Alfier, F. Bonomo, P. Franz, P. Innocente, and R. Pasqualotto, "Enhanced confinement and quasi-single-helicity regimes induced by poloidal current drive," *Phys. Rev. Lett.* **99**, 095001 (2007).
- ⁵⁴M. E. Puiatti, S. Cappello, R. Lorenzini, S. Martini, S. Ortolani, R. Paccagnella, F. Sattin, D. Terranova, T. Bolzonella, A. Buffa, A. Canton, L. Carraro, D. Escande, L. Garzotti, P. Innocente, L. Marrelli, E. Martines, P. Scarin, G. Spizzo, M. Valisa, P. Zanca, V. Antoni, L. Apolloni, M. Bagatin, W. Baker, O. Barana, D. Bettella, P. Bettini, R. Cavazzana, M. Cavinato, G. Chitarin, A. Cravotta, F. D'Angelo, S. D. Bello, A. D. Lorenzi, D. Desideri, P. Fiorentin, P. Franz, L. Frassinetti, E. Gaio, L. Giudicotti, F. Gnesotto, L. Grando, S. Guo, A. Luchetta, G. Malesani, G. Manduchi, G. Marchiori, D. Marcuzzi, P. Martin, A. Masiello, F. Milani, M. Moresco, A. Murari, P. Nielsen, R. Pasqualotto, B. Pégourie, S. Peruzzo, R. Piovano, P. Piovesan, N. Pomaro, G. Preti, G. Regnoli, G. Rostagni, G. Serianni, P. Sonato, E. Spada, M. Spolaore, C. Taliervo, G. Telesca, V. Toigo, N. Vianello, P. Zaccaria, B. Zaniol, L. Zanotto, E. Zilli, G. Zollino, and M. Zuin, "Analysis and modelling of the magnetic and plasma profiles during PPCD experiments in RFX," *Nucl. Fusion* **43**, 1057–1065 (2003).
- ⁵⁵S. Cappello, "Bifurcation in the MHD behaviour of a self-organizing system: The reversed field pinch (RFP)," *Plasma Phys. Controlled Fusion* **46**, B313 (2004).
- ⁵⁶S. Cappello, D. Bonfiglio, D. F. Escande, S. C. Guo, A. Alfier, and R. Lorenzini, "The reversed field pinch toward magnetic order: A genuine self-organization," *AIP Conf. Proc.* **1069**, 27–39 (2008).
- ⁵⁷D. Bonfiglio, M. Veranda, S. Cappello, D. F. Escande, and L. Chacón, "Experimental-like helical self-organization in reversed-field pinch modeling," *Phys. Rev. Lett.* **111**, 085002 (2013).
- ⁵⁸M. Veranda, D. Bonfiglio, S. Cappello, D. F. Escande, F. Auremma, D. Borgogno, L. Chacón, A. Fassina, P. Franz, M. Gobbin, D. Grasso, and M. E. Puiatti, "Magnetohydrodynamics modelling successfully predicts new helical states in reversed-field pinch fusion plasmas," *Nucl. Fusion* **57**, 116029 (2017).
- ⁵⁹D. Bonfiglio, M. Veranda, S. Cappello, D. F. Escande, G. D. Giannatale, A. Kryzhanovskyy, M. Veranda, L. Marrelli, and P. Zanca, "Effect of a realistic boundary on the helical self-organization of the RFP," in *46th European Physical Society Conference on Plasma Physics*, Milan, Italy (Curran Associates, Inc., 2019).

⁶⁰D. Bonfiglio, S. Cappello, L. Chacón, D. F. Escande, G. D. Giannatale, A. Kryzanovskyy, M. Veranda, L. Marrelli, and P. Zanca, “Nonlinear MHD modelling of helical self-organization in the RFP: Effect of a realistic boundary and predictions for RFX-mod2,” 3rd Asia-Pacific Conference, Hefei, China, 2019.

⁶¹The Tokamak Disruption Simulation SciDAC Team, “Tokamak disruption simulation project,” <https://tds-scidac.github.io/gallery/> (accessed 28 July 2023).

⁶²D. Schnack, D. Barnes, Z. Mikic, D. S. Harned, and E. Caramana, “Semi-implicit magnetohydrodynamic calculations,” *J. Comput. Phys.* **70**, 330–354 (1987).